Deformability of *Plasmodium falciparum* Parasitized Red Blood Cells

by

John Philip Mills

B.S., Materials Science and Engineering,
Cornell University (2001)

Submitted to the Department of Materials Science and Engineering
in partial fulfillment of the requirements for the degree of

Doctor of Philosophy in Materials Science and Engineering

at the

MASSACHUSETTS INSTITUTE OF TECHNOLOGY

February 2007

Author ....
Department of Materials Science and Engineering
January 17, 2007

Certified by ....
Subra Suresh
Ford Professor of Engineering
Thesis Supervisor

Accepted by ....
Samuel M. Allen
POSCO Professor of Physical Metallurgy
Chair, Departmental Committee on Graduate Students

Deformability of *Plasmodium falciparum* Parasitized Red Blood Cells

by

John Philip Mills

Submitted to the Department of Materials Science and Engineering
on January 17, 2007, in partial fulfillment of the
requirements for the degree of
Doctor of Philosophy in Materials Science and Engineering

Abstract

The biophysical properties of the human red blood cell (RBC) permit large deformations required for passage through narrow capillaries and spleen sinusoids. Several pathologic conditions alter RBC deformability that can result in abnormal circulation behavior. In the present work, altered RBC deformability caused by invading *Plasmodium falciparum* parasites, which are responsible for the disease malaria, is evaluted. *P. falciparum* parasitized RBCs (pRBCs) display decreased deformability and novel cytoadherence properties, and sequester in the microcirculation. Parasite-exported proteins that interact with the pRBC membrane are identified as the cause for these alterations. It is postulated that sequestration of pRBCs is responsible for severe cases malaria. Previous studies of pRBC deformability could not characterize deformability over all parasite intra-erythrocytic developmental stages due to experimental limitations. In the present work, a technique based on optical tweezers is developed to permit testing of pRBC deformability over all intra-erythrocytic stages. Optical tweezers can measure the force versus displacement response of a single RBC in uniaxial tension. The membrane shear modulus, which is a major factor in determining overall RBC deformability, can be interpreted based on the single RBC force versus displacement response. Initial tests with optical tweezers conducted on healthy RBCs demonstrate that shear modulus values were consistent with accepted values from standard techniques. Next, deformability of *P. falciparum* pRBCs was measured at all intra-erythrocytic parasite developmental stages. Deformability is found to decrease ten-fold during parasitization, which is three to four times greater than previously estimated. Finally, optical tweezers experiments are combined with targeted gene disruption techniques to measure the effect of a single parasite-exported protein on pRBC deformability. It is shown that Ring–infected Erythrocyte Surface Antigen (RESA), a membrane binding parasite-exported protein, plays a major role in reducing deformability of pRBCs at the early stages of intra-erythrocytic parasite development. Furthermore, the effect of RESA on deformability is more pronounced at febrile temperature, which early stage pRBCs can be exposed to during a malaria attack, than at normal body temperature.

Thesis Supervisor: Subra Suresh
Title: Ford Professor of Engineering

Acknowledgments

First, I acknowledge my advisor Prof. Subra Suresh for his support and guidance throughout the duration of my graduate program. Through his leadership and dedication to scientific research, I was afforded many unique experiences to conduct research projects involving international collaboration with other leading research institutions. For his devoted commitment to my success as a graduate student at MIT and to my future scientific career, I extend my utmost gratitude to Prof. Subra Suresh.

I am extremely grateful for my interactions with Prof. Lorna J. Gibson. As a member of my thesis committee, she provided insightful evaluation of my research. Her continuous support and interest in my projects were always appreciated. In addition, as her teaching assistant for two graduate courses, I gained invaluable experience and insight regarding academic classes and lecturing.

I am appreciative of Prof. Ram Sasisekharan who served on my thesis committee. His insight and understanding of my research topic were extremely inspiring and helpful.

In addition, I thank Prof. Christine Ortiz for serving on my thesis committee during my final defense.

I extend tremendous gratitude to Dr. Monica A. Diez Silva and David J. Quinn for their significant contributions to the research projects presented in this thesis. Monica's keen scientific perception and understanding of *Plasmodium falciparum* and RESA were critically important for topics addressed in this thesis. David's dedication to the design, construction and calibration of the optical tweezers instrument described in Section 3.2.2 is deeply appreciated.

I acknowledge the help of Prof. Matthew J. Lang and his research group for the development of the optical tweezers instruments described in Chapter 3. Particular appreciation is given to Ricardo Brau for his helpful discussions while developing the optical tweezers instrument described in Section 3.2.1 and his commitment to the design and construction of the instrument described in Section 3.2.2. Other members of the group, Jorge Ferrer, David Appleyard, Peter Lee, Dr. Peter Tarsa, and Carlos Castro are also acknowledged for their continual help. During early development of the optical tweezers instrument described in Sections 3.2.2, I acknowledge the help of Prof. Kevin T. Turner and Anna Chen.

For the computational modeling simulations used to interpret experimental data, I acknowledge the substantial work of Dr. Ming Dao, a research scientist in Prof. Suresh's research group, and Prof. Ju Li at The Ohio State University.

I am extremely grateful for the opportunity to complete research projects presented in Chapters 4 and 5 at the National University of Singapore in the laboratory of Prof. Chwee Teck Lim, who served as a second advisor. Interactions with Prof. Kevin S. W. Tan and his laboratory were instrumental for the projects involving *Plasmodium falciparum.* The help of Prof. Chorng-Haur Sow and Gregory Lee for preparing the optical tweezers instrument in the laboratory of Prof. Lim is very much appreciated. The assistance of Qie Lan for her help in testing reported in Chapters 4 and 5 and helpful discussions with Dr. Enhua Zhou are acknowledged.

The collaboration and extremely significant contributions of Prof. Geneviève Milon, Prof. Peter H. David, M.D., Prof. Odile Mercereau-Puijalon and Prof. Serge Bonnefoy at the Institute Pasteur are kindly acknowledged. These interactions evolved from the Ph.D. work of Dr. Monica A. Diez Silva while at Institute Pasteur. I am especially thankful for the very helpful discussions and interactions with Prof. Milon and Prof. David during their visits to MIT.

I extend deep appreciation to Ken Greene and George LaBonte who support the entire laboratory of Prof. Subra Suresh. Ken and George have been of great help throughout my time in the laboratory.

As an undergraduate at Cornell University, many professors were influential in my early development as a scientist. I acknowledge Prof. Stephen L. Sass, Prof. Shefford Baker, Prof. Michael Thompson, Prof. George Malliaras, Prof. Christopher Ober and Prof. Alan Zhender for stimulating my interest in research and academia. Prof. Timothy S. Fisher, currently at Purdue University, provided particular motivation that directly led to my success as a student at Cornell University.

I would also like to acknowledge the following people at MIT and various other institutions for their helpful academic interactions: Dr. Tim Hanlon, Dr. Nuwong (Kob) Chollacoop, Prof. Krystyn Van Vliet, Dr. In-suk Choi, Prof. Pasquale D. Cavaliere, Prof. Trevor Lindley, Dr. Ruth Schwaiger, Prof. Sam Allen, Prof. Roger Kamm, Prof. Alan Grodzinsky, Li Ang, Dr. Marina Puig-de-Morales, Dr. George Lykotrafitis, Dr. Gerrit

Huber, Irene Chang, Nadine Walter, Dr. Alexandre Micoulet, Andrea K. Bryan, Anamika Prasad, Dr. Suliana Manley, Dr. Margaret Horton, Joe Walish, Solar C. Olugebefola, Lisa Joslin, Tiffany S. Santos, Alec P. Robertson, David Danielson, G.J. la O', Grace Y. Kim, Robert D. Boyer, Prof. Megan Frary, Joost Bonsen, Karl Ruping, John Lock, David Robertson, Coleman Greene, Kevin R. Duda, Kevin M. Maloney, William Ouimet, Dan Burns, Dr. Brad Peterson, Scott Litzelman, Julie Cheng, Angelita Mireles, Kathy Farrell, Stephanie Bright and Ada Ziolkowski.

And the most profound thanks to my parents and my brother.

Contents

List of Figures

Chapter 1

Introduction

Mechanical properties of the human red blood cell (RBC) allow for repeated large elastic deformations while circulating continuously *in vivo.* Severe complications can result when the deformability of RBCs is compromised due to pathologic conditions. A variety of blood disorders are known to modify RBC structure thereby altering mechanical properties of the membrane and, consequently, altered or insufficient blood circulation. Hereditary disorders such as spherocytosis, elliptocytosis ovalocytosis [11–13] and sickle cell disease [14–16], and infectious diseases such as malaria [7, 17] are all known to involve significant changes to the deformability properties of RBCs. In addition to the altered deformability of the RBC, changes to cytoadherence are also known to occur as a consequence of ultrastructure changes engendered by disease states [17].

Mechanical property measurement of pathologic RBCs at the single-cell level poses technical challenges because of the small length-scales (μm) and forces (picoNewton, pN) needed to study RBC deformability by recourse to continuous records of force versus deformation. In turn, the changes to deformability of pathologic RBCs are typically not completely characterized despite extensive knowledge of the biochemical composition of these cells. In this thesis, measurement of RBC deformability is applied to the study of changes caused by RBC parasitization by *P. falciparum.* For the case of *Plasmodium falciparum* parasitized RBCs, it is known that significant changes to deformability properties result in sequestration of parasitized RBCs in small capillaries thereby causing decreased

O_2 perfusion to surrounding tissues [2]. It is postulated that such sequestration and destruction of parasitized RBCs could be implicated in life-threatening cases of severe malaria. While adhesion properties of *P. falciparum* parasitized RBCs have been studied, much less is known about deformability changes induced by the parasite. For example, the standard technique of micropipette aspiration that is used to measure deformability of RBCs has technical limitations that prevent deformability measurements of *P. falciparum* parasitized RBCs at the mature stages of parasite development when sequestration occurs.

To study the deformability of *P. falciparum* parasitized RBCs at the single-cell level over all stages of intra-erythrocytic parasite development, two new optical tweezers experimental techniques were developed. Results extracted from the optical tweezers technique were shown to be consistent with accepted results from micropipette aspiration experiments for healthy RBCs, while providing significantly enhanced capabilities for probing the mechanical properties of pathologic cells in a controlled and quantitative manner. The new optical tweezers instruments were used to measure the deformability of parasitized RBCs over all parasite development stages. In addition, the optical tweezers technique was coupled with gene disruption techniques to study protein-level effects on deformability.

In Chapter 2, background information on healthy RBC deformability is provided along with a description of intra-erythrocytic development of *P. falciparum* and associated deformability changes.

Methods of both optical tweezers techniques are provided in Chapter 3.

Results are presented in Chapter 4 on elastic and viscoelastic properties of healthy RBC membranes and compared to accepted values based on micropipette aspiration experiments. Next, Chapter 5 presents results on the deformability of *P. falciparum* parasitized RBCs over all intra-erythrocytic parasite developmental stages. In Chapter 6, the effect of parasite exported protein RESA, which interacts with the RBC membrane, is characterized.

Major conclusions of this thesis are presented in Chapter 7.

Chapter 2

Background

2.1 Red Blood Cell Deformability

The deformability of human RBCs is critically important for normal *in vivo* circulation required for transport of O_2 and CO_2. The resting biconcave discocyte shape of a RBC (8 μm in diameter and 2.5 μm in thickness, on average) must quickly and reversibly accommodate large deformations when passing through narrow capillaries as small as 2 μm in diameter. The RBC membrane can experience strains higher than 100% and shear forces in excess of 100 pN [18]. During the approximate 120 day lifespan, RBCs can circulate up to half a million times through narrow capillaries and spleen sinusoids. Aged RBCs with decreased deformability can be detected and removed by macrophages in the spleen [1].

The RBC consists of an outer membrane that surrounds the cytosol fluid containing hemoglobin for gas transport. The low viscocity of the cytosol and high surface–to–volume ratio of the biconcave shape facilitate large deformations of the RBC [17]. The other key property for RBC deformability is the highly elastic membrane that supports shear forces during large deformation.

The superstructure of the RBC membrane is illustrated in Figure 2-1 and consists of an outer phospholipid bilayer and supporting associated cytoskeletal spectrin network. The biochemical composition of the membrane is well characterized. The phospholipid bi-

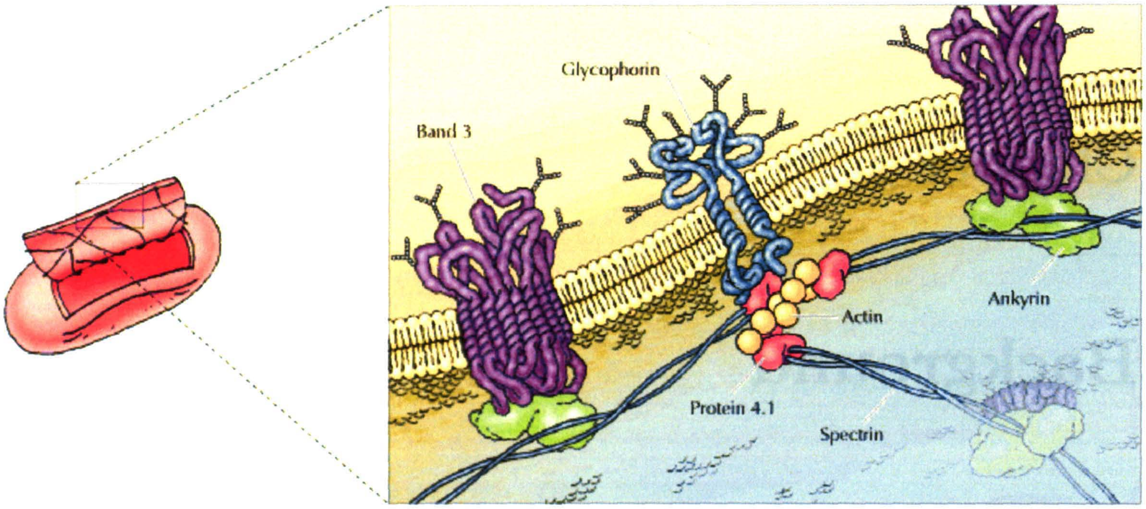

Figure 2-1: A schematic representation of the RBC membrane. Illustration from Alberts *et al.* [1]

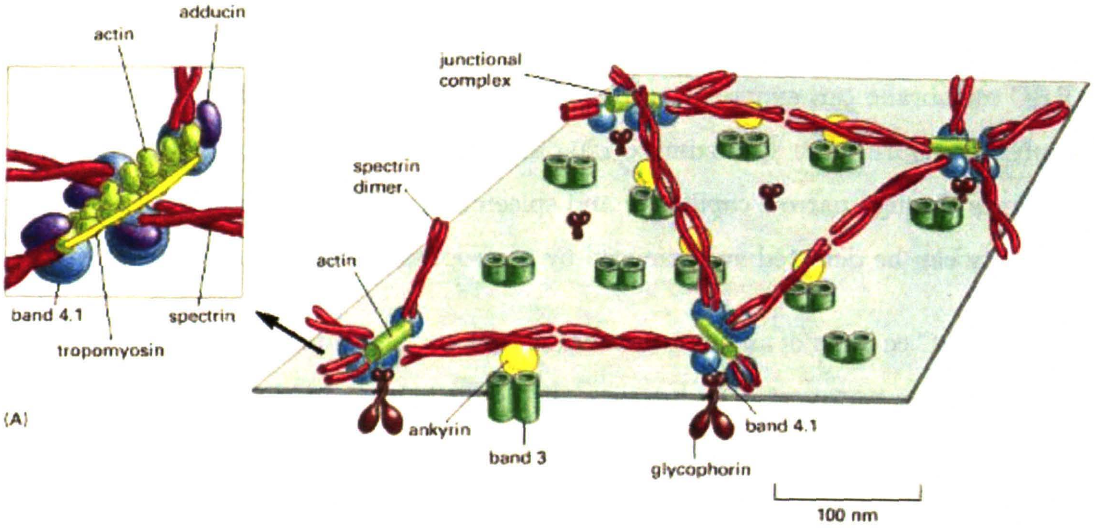

Figure 2-2: The spectrin network cytoskeleton shown schematically. Image from Alberts *et al.* [1].

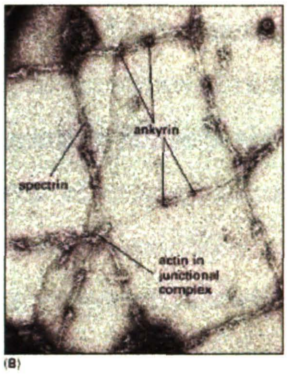

Figure 2-3: The spectrin network cytoskeleton shown in an electron micrograph. Image from Alberts *et al.* [1].

layer contains cholesterol molecules and integral proteins to which the spectrin network is attached. The polar nature of the phospholipid molecules imparts area conservation and some amount of bending rigidity to the RBC. However, the bilayer can not support shear forces that occur during deformation through narrow capillaries and spleen sinusoids. The shear resistance is derived mainly from the spectrin network which is shown schematically in Figure 2-2. Spectrin heterodimers, which consist of intertwined α and β spectrins, associate head–to–head to form tetramers. At each end of the tetramer, f–actin and band 4.1 form junctional complexes that link spectrin tetramers together to for the two–dimensional cytoskeletal network. The junctional complexes are connected by integral protein glycophorin to the phospholipid bilayer. Band 3 and and ankyrin form a complex that also anchors the spectrin network to the phospholipid bilayer. Collectively, the composite properties of the phospholipid bilayer and spectrin network combine to give the unique elastic properties of the membrane. The importance of RBC superstructure to membrane deformability is highlighted by membrane cytoskeleton defects that alter normal RBC circulation behavior. For the cases of spherocytosis, elliptocytosis and ovalocytosis, defects in the spectrin network lead to loss of normal biconcave shape and decreased capacity for deformation [11–13].

For healthy RBCs, the composite properties of the phospholipid bilayer and associated spectrin network have been characterized by various techniques. The bending modulus, B_0, has been measured to be in the range of $1.7 \times 10^{19} - 9 \times 10^{19}$ N·m [19, 20]. The area expansion modulus, K, measured by micropipette aspiration is found to be $300-500$ mN/m

[21–24]. Also measured by micropipette aspiration, the shear modulus of the RBC membrane is $4 - 10$ μN/m. The strong resistance of the phospholipid bilayer to change in area causes the area expansion modulus to be orders–of–magnitude larger than the shear modulus. It has been demonstrated that the bending modulus does not contribute significantly to the large deformation response in comparison to the shear modulus [25]. For these reasons, it is known that the shear modulus, which is a property related to the spectrin network, of the RBC membrane is the major factor in determining overall RBC deformability [21].

Mechanical response of RBCs has long been studied by means of the micropipette aspiration method (e.g., [26, 27]) whereby a single cell is aspirated into a glass tube by application of suction pressure. From comparisons of geometry changes of the aspirated cell with that predicted from analytical and numerical models of deformation, its elastic response during the application of the pressure and its viscoelastic relaxation response upon release of pressure are estimated. Two main limitations of micropipette aspiration are the complex stress state that makes interpretation difficult and that only a portion of the cell membrane can be sampled. Furthermore, for the case of *P. falciparum* parasitized RBCs, the increased adhesion of these cells causes increased friction along the inner wall of the micropipette which complicates interpretation of these results. Well-defined stress states can in theory be applied to an entire RBC without complications due to friction by implementation of optical tweezers.

Direct tensile stretching of the human RBC using optical tweezers to extract elastic properties was first reported by Hénon *et al.* [28] who attached two silica beads non-specifically to diametrically opposite ends of the cell, trapped both beads with laser beams, and imposed tensile elastic deformation on the cell by moving the trapped beads in opposite directions. Forces were calibrated by subjecting a trapped bead to counter flow following the procedures outlined by Svoboda and Block [3] and Simmons *et al.* [29]. Stokes law was used to estimate the force on the trapped bead from known fluid velocity. With a 1.064 μm Nd:YAG laser beam of 605 mW maximum emission power and silica beads 2.1 μm in diameter, they imposed maximum tensile forces that were estimated to be 56 pN on discocytic and osmotically swollen, nearly spherical cells. By employing simple analytical expressions based on two-dimensional linear elastic, small deformation, idealization of the cell, they examined variations in only the transverse diameter of the cell with applied force, and ignored possible contributions to deformation arising from the bending stiffness of the cell membrane and cytoskeleton. Finite contact between the beads and the cell membrane during stretching by optical tweezers was also not considered. The in-plane shear modulus of the cell membrane was estimated from this approach to be 2.5 ± 0.4 μN/m. This estimate is lower than the range of shear modulus values of 4 to 10 μN/m obtained from a number of independent investigations which employed the more commonly known micropipette aspiration technique [20, 26, 30, 31]. Studies by the same group [32] employing triple bead optical tweezers measurements showed that the area expansion modulus and shear modulus of RBCs were higher in an isotonic buffer than in a low hypotonic buffer.

Sleep *et al.* [33] also estimated elastic properties of the human red blood cells by optical tweezers where two polystyrene latex beads of 1 μm diameter were trapped using a 1.047 μm Nd:YLF laser beam. In this experiment, one bead was held fixed and the other moved with a second trap to induce tensile deformation in the cell. Trap stiffness was estimated from the Brownian motion of the trapped bead. The variation of imposed force, up to a maximum of 20 pN, as a function of the transverse diameter, was reported for permeabilized spherical ghost cells whose deformation at a given force was about one half that of discocytic and osmotically swollen spherical cells. By invoking an axisymmetric cell model of Parker and Winlove [34], they estimated the in-plane shear modulus from optical tweezers studies to be nearly two orders of magnitude larger than those reported by Hénon *et al.* [28]. The analyses of deformation for extracting elastic properties also invoke rather severe assumptions on cell shape (e.g., idealization of a biconcave cell as a two-dimensional planar disc by Hénon *et al.* [28], and neglect of the effects of the relatively large contact region between the cell and the beads in this study and in the one by Sleep *et al.* [33]). These theoretical assumptions along with possible errors arising from variations in force calibration procedures could account for the disparity between the initial optical tweezers based shear modulus values and accepted values based on standard techniques.

All of the foregoing studies of cell deformation by optical tweezers involve primarily small elastic deformation at low applied forces. Studies of deformation conditions at larger strain levels inevitably require much higher forces, which are conceptually feasible to obtain using the optical tweezers method. In fact, a study of unfolding of titin molecules by Kellermayer *et al.* [35] reported an estimated stretching force in excess of 400 pN using optical tweezers where a 1046 nm Nd:YAG laser with a maximum power of 1.5 W was used to trap a 3 μm diameter latex bead and where the force calibration was performed using the Stokes law method.

In principle, the optical tweezers method affords several potential advantages for the study of deformation of single biological cells:

- It provides a means to impose simple and well-controlled stress states, such as direct tensile stretching in small or large deformation, to biological cells. In this sense, it is complementary to, and conceptually simpler to interpret than, the widely used micropipette aspiration method [18, 20].
- The stress state imposed on the cell can be systematically varied by employing multiple beads which are attached to cell membranes, whereby the constitutive response of the cell membrane and cytoskeleton can be probed for different chemical and biological conditions.
- Optical tweezers stretching of cells in one or more directions is also amenable to three-dimensional computational simulations which can be used to guide and interpret experimental observations.
- The relaxation response of the stretched cell upon release of the tensile stretch in the optical tweezers experiments can also be used to extract the viscoelastic response of the cell.
- This method further provides a possible means to investigate systematically the effects of the progression of a pathological state, such as *Plasmodium falciparum* parasitized RBCs, on the deformation characteristics and elastic and viscoelastic properties of the cell membrane [6]. Possible complications arising from micropipette aspiration of such infected cells, such as stress concentration at the ends of the micropipette and adhesion of the infected cell to the inner walls of the micropipette, can potentially be circumvented in the optical tweezers method.

Despite these advantages, uncertainties exist in the calibration of the force imposed on the cell by the optical tweezers method, which is in the pN to several hundred pN range.

Such complications have led to considerable variation and scatter in the experimental data reported previously in the literature. A comparison of the optical tweezers method with other techniques available for the study of mechanics of single cells and populations of cells can be found in recent reviews [36, 37].

2.2 *P. falciparum* Parasitized Red Blood Cell Deformability

Among the four different species of *Plasmodium* that can parasitize human RBCs, *P. falciparum* and *P. vivax* are the most common, with the former resulting in more severe form of malaria [2]. Malaria induced by *P. falciparum* is the most widespread parasitic disease in humans with an estimated annual infection rate of several hundred million people worldwide and an estimated annual mortality rate of several million, mostly children. The intra–erythrocytic stage of *P. falciparum* occurs after the parasite (merozoite) leaves the liver to invade RBCs, and during the subsequent asexual stage lasting about 48 h, the parasite nucleates inside the RBC to producing up to 20 new merozoites 2-4. Each merozoite can subsequently invade other healthy RBCs.

When a merozoite invades an RBC, it undergoes pronounced structural changes within the RBC. The intra–erythrocytic developmental stages of the parasite are broadly classified as:

- ring stage: with characteristic thin discoidal, flat or cup-shaped ring features whose formation commences at about 30 min from the time of invasion of the parasite into the RBC
- trophozoite stage: with irregular bulges or knobs at the surface of the parasite appearing at about 24 h after invasion, parasite growth inside the RBC and formation of small pigmented regions, and
- schizont stage: with nuclear division of the parasite resulting in the multiplication of the number of merozoites, greater spread of parasite and pigmented regions within cell volume, and export of parasite proteins to the RBC membrane causing severe distortion of the cell cytoskeleton and membrane some 3648 h after invasion.

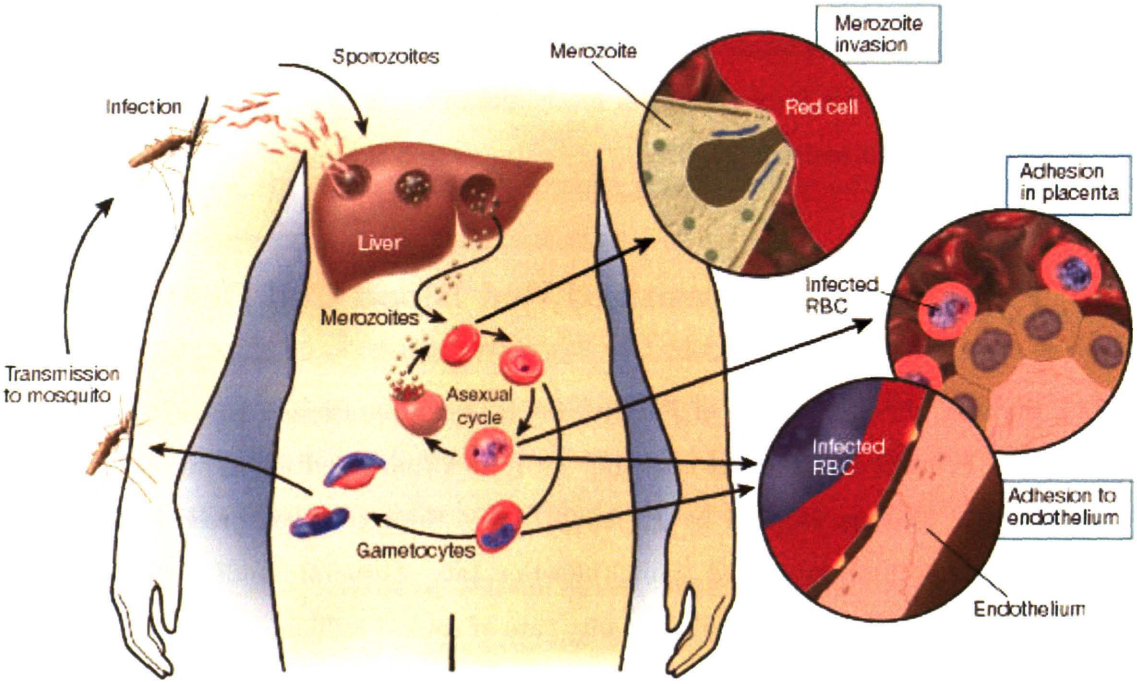

Figure 2-4: The *P. falciparum* parasite life-cycle. Illustration from Miller [2].

In the late schizont stage, the parasitized RBC also exhibits a change in shape, which is spherical compared to the biconcave shape for the healthy RBC.

Reviews of structure evolution during these developmental stages has been previously reported [2, 17, 38].

An important outcome of the full development of *P. falciparum* within the RBC is that it increases the adhesion of infected RBCs to inner linings of small blood vessels. Single-cell mechanical property measurements performed using the micropipette aspiration method [39, 40] and the laminar shear flow method [8] also show that RBCs parasitized by *P. falciparum* stiffen considerably with marked increases in their shear moduli. Profound alterations to the mechanical properties and adhesive response of the parasitized RBCs cause them to sequester in the microvasculature of major organs. Life-threatening consequences of such sequestration can include cerebral malaria, hypoglycaemia, metabolic acidosis and respiratory distress [2].

What has not been shown is loss of deformability at all adhesive stages of trophozoite and schizont when change in deformability properties could have an effect on sequestration. It has been shown that for *P. vivax* that parasitized RBCs do not stiffen and do not have adhesion properties like *P. falciparum*. *P. vivax*, consequently, does not become sequestered and is generally regarded as not being lethal like *P. falciparum*.

Chapter 3

Methods

3.1 Overview

The single cell force–displacement response of RBCs is determined by two different methods, each developed as part of this project, that employ the optical tweezers technique of direct RBC stretching: an escape force method and a trap stiffness method. The former method is based on the escape force needed to dislodge a bead from the optical trap. The latter method involves tracking the position of a bead within the optical trap; the relationship between force and bead position is calibrated prior to experiments. The escape force method requires a less complicated experimental set-up, but significant post-processing of data; the trap stiffness method has a complicated experimental layout that requires fine alignment of optical components, but provides a higher degree of accuracy in force and displacement measures and has significant automation to conduct tests and acquire data in real-time. The escape force method is used to measure the force–displacement response of healthy and *P. falciparum* parasitized RBCs in Chapters 4 and 5. The trap stiffness method, is used to obtain results on genetically disrupted *P. falciparum* parasitized RBCs presented in Chapter 6.

The overall approach of the optical tweezers method begins by attaching beads to specific locations on the RBC membrane. Calibrated pN–level forces generated by optically trapping the beads attached to the cells (either specifically or non-specifically) are used

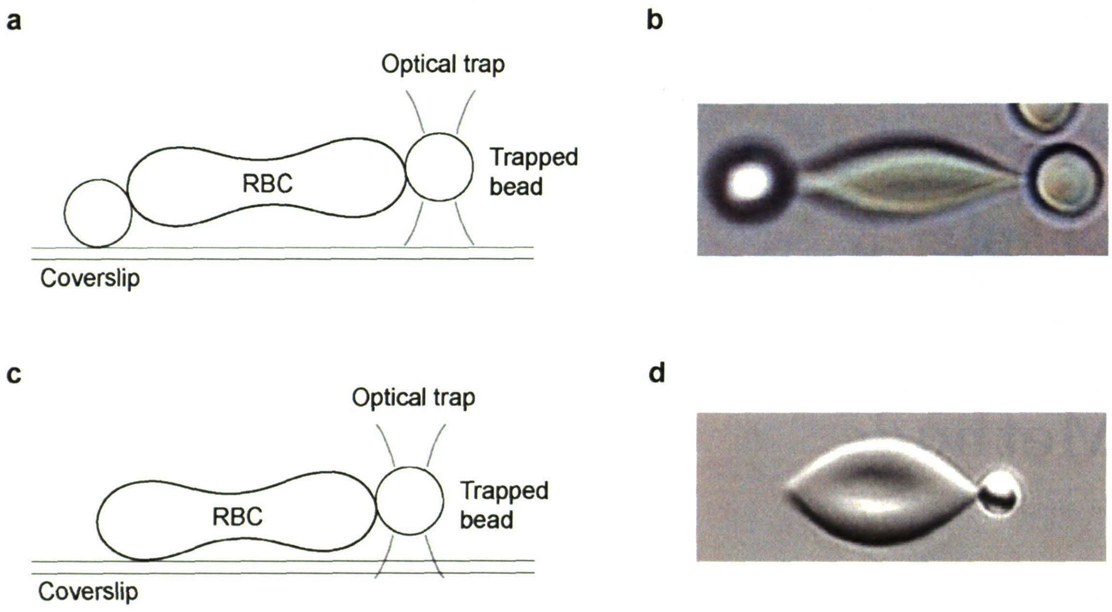

Figure 3-1: Test configurations for optical tweezers uniaxial tension experiments are shown. (**a**) and (**c**) are schematic representations of two possible experimental geometries. In (**a**), the RBC is attached to two beads at diametrically opposite ends, with one bead optically trapped above the surface and the other bead adhered to the coverslip. The contact points on the RBC serve as grips to stretch the cell. In (**c**) an alternate geometry is used to attached the RBC directly to the coverslip at one small region instead of using a bead as in (**a**). In (**b**) and (**d**), a top view of test configuration (**a**) and (**c**), respectively, is shown. (**b**) and (**d**) show RBC under some amount of uniaxial loading. Scale: (**b**) beads are 4 μm in diameter and (**d**) the bead is 2 μm in diameter.

to deform single RBCs. By monitoring the displacements of an RBC under calibrated forces, the force–displacement response can be experimentally determined. Details of the two optical tweezers methods are provided in Sections 3.2.1 and 3.2.2.

3.2 Optical Tweezers Experiments

The single cell force–displacement response of RBCs is experimentally measured by the optical tweezers method. The two test configurations used for uniaxial tension tests are shown in Figure 3-1. In Figure 3-1a, an RBC is attached to two beads at diametrically opposite locations on the membrane. The position of the bead attached to the coverslip

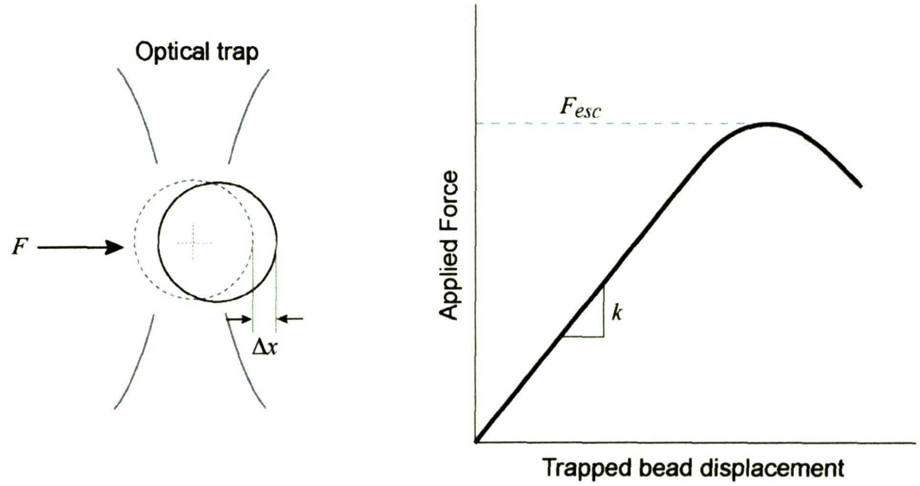

Figure 3-2: The schematic of an applied force exerted on an optically trapped bead is shown (**left**). The equilibrium position of the trapped bead under no applied force is shown by the dotted bead in the center of the optical trap. The applied force displaces the trapped bead from the center. The plot (**right**) indicates the optically trapped bead position (Δx) as a function of applied force (F) for a given incident laser power. The position of the bead relative to the optical trap center is proportional to the applied force for small displacements and is characterized by a trap stiffness, k. The force at which a bead will just escape the trap is defined as the escape force, F_{esc}. The magnitude of the trap stiffness and escape force scale proportionately with incident laser power.

can be controlled by movement of a motorized microscope stage to accurately position the sample. The other bead is optically trapped above the coverslip surface. In the other test configuration illustrated in Figure 3-1c, a small portion of the RBC membrane is attached directly to the coverslip on the left side of the RBC as shown. Contact points on opposite sides of the RBC serve as grips to stretch the cell in uniaxial tension.

The force–displacement test is performed by moving the stage to apply deformations while forces are measured by either the escape force method or trap stiffness method. Figure 3-2 illustrates the equilibrium position of a trapped bead as a function of increasing levels of applied force for a constant trapping laser power. The force exerted by the trap scales proportionately with trapping laser power. The escape force method (Sec. 3.2.1) is based on calibrating the maximum trap force (escape force, F_{esc}, Fig. 3-2) at different trapping laser powers. Using various trapping laser powers, a range of calibrated forces can be exerted on an RBC. The trap stiffness method (Sec. 3.2.2) involves calibrating the linear region of the equilibrium trapped bead position versus applied force (Fig. 3-2). The position of a bead within the trap is determined by a separate laser-based position detection system. Position detection involves a second low-powered laser in the same path as the trapping laser, but that has a different wavelength and does not contribute significantly to trapping forces. The signal of the detection laser after passing through a trapped bead is imaged onto a position-sensitive diode (PSD). The PSD signal can be used to continuously measure the position of a trapped bead in real-time. After calibration of the trap stiffness, the force during a trap stiffness method experiment can be detected continuously by tracking the trapped bead position with the laser-based position detection system. Therefore, the force–displacement curve can be obtained from a single stretch at a given laser power with the trap stiffness method.

The first experiments reported in Chapters 4 and 5 were conducted using the escape force method. This technique required a relatively simple experimental set-up and permitted force–displacement data collection with substantial post-processing effort. The trap stiffness method represents a refinement of the initially developed escape force method. The design of the trap stiffness method permits more accurate force–displacement measurement and more automated testing, while requiring significantly more precise alignment and calibration of all components. The trap stiffness method, completed after results were obtained for Chapters 4 and 5, was used for results presented in Chapter 6.

3.2.1 Escape Force Method

The escape force optical tweezers method is illustrated in Figure 3-3 and described in more detail in Mills *et al.* [4]. The design incorporates an inverted microscope (Leica Microsystems, Wetzlar, Germany) and a trapping laser module (1064 nm Nd:YAG, 1.5 W, LaserTweezers, Cell Robotics, Inc.) to form a single-bead gradient optical trap. The trap is formed by focusing the laser through an oil immersion lens (100× magnification) which is also used to view the sample during tests. Optically trapped silica beads (4.12 μm in diameter, Bangs Laboratories, USA) attached to an RBC (Fig. 3-1a) were used to apply calibrated forces to the cell. The relatively high laser power and large bead diameter

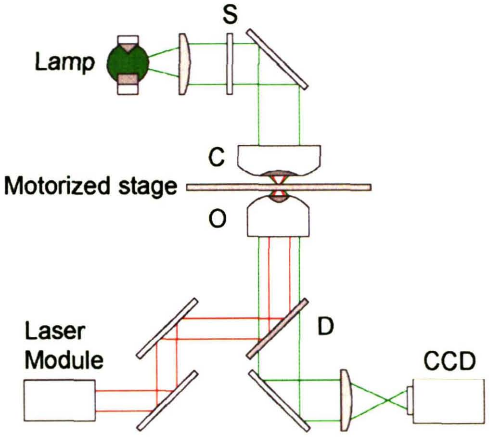

Figure 3-3: The optical design layout is shown for the escape force method optical tweezers instrument. The optical trap is formed by focusing the beam from the laser module (pathway shown in red) with the objective (O), which is also used to image the experiment with the microscope illumination (pathway shown in green). A CCD camera records RBC deformation experiments for post-test analysis. Not all components are shown. (C, condenser; S, shutter; D, dichroic mirror)

facilitate exertion of forces on the cell that are about three to six times greater than those reported by similar earlier studies [28, 33]. The large forces are used to measure nonlinear single RBC force–displacement response and viscoelastic recovery.

Force calibration

Calibration of the optical tweezers instrument is performed by an escape force method [3]. In this technique, which is referred to as the stage movement technique, the force required to displace a trapped bead out of the optical trap is measured by applying a known viscous drag force by moving a motorized stage. The calibration procedure begins by trapping a bead in solution (phosphate-buffered saline (PBS) with 0.1 mg/ml bovine serum albumin (BSA)) at a measured height ($h = 3$ μm) above the coverslip surface. The solution and height of the trapped bead above the slide surface are kept unchanged throughout calibration and experimental tests. As the microscope stage is moved at a specified velocity, the fluid exerts a viscous drag force on the trapped bead, as shown in Fig. 3-4. The viscous drag force, F_d, equals the magnitude of the escape force, F_{esc}, when the bead just escapes the trap. From the stage velocity, v_{esc}, at the point of escape, the escape force is estimated

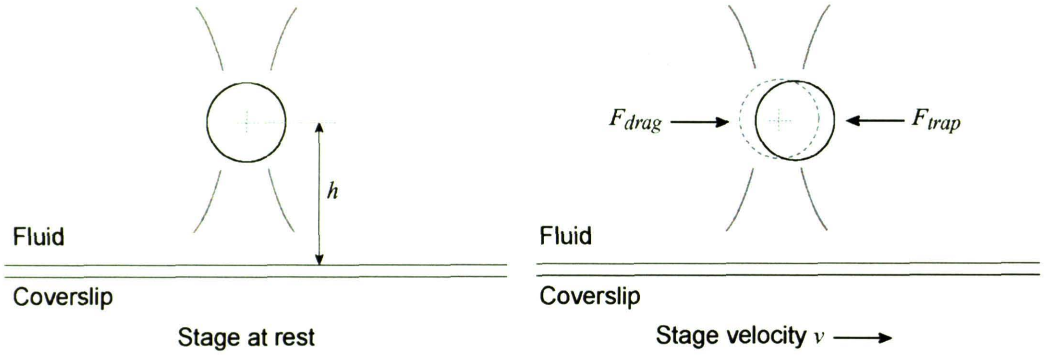

Figure 3-4: Calibration of the optical trap using an escape force method [3]. A silica bead, 4.12 μm in diameter, is trapped in fluid (PBS and bovine serum albumin, BSA) at a measured height, $h = 3$ μm, above the slide surface. As the microscope stage and fixed slide are translated, the fluid exerts a viscous drag force on the trapped bead. When the viscous drag force is just equal to the escape force, the bead will escape the trap.

as

$$F_{esc} = |F_d| = \beta v_{esc} \tag{3.1}$$

The viscous drag coefficient, β, for a spherical bead located near a wall is described by Faxens Law [3],

$$\beta = \frac{6\pi\eta r}{(1 - \frac{9}{16}(r/h) + \frac{1}{8}(r/h)^3 - \frac{4}{256}(r/h)^4 - \frac{1}{16}(r/h)^5} \tag{3.2}$$

where, for the reported experiments, the bead radius, $r = 2.06$ μm, height of the bead above the wall, $h = 3$ μm, and fluid viscosity, $\eta = 0.0013$ Pa·s. Equation 3.1 takes the form of Stokes' law, $F = 6\pi r\eta v$, for a bead located far from the coverslip.

The stage movement technique described here represents an extension of fluid chamber technique used in previous work [25, 41]. The fluid chamber technique imposes a viscous drag force by flowing fluid through a narrow channel where a bead is trapped. Fluid velocity, estimated by tracking the speed of untrapped beads, is used with Equation 3.1 to determine the escape force. However, this calibration method has some significant limitations. First, untrapped beads used to determine fluid velocity flow at various heights above the coverslip that may not be consistent with the velocity in Equation 3.1. Untrapped beads tend to flow along the surface of a slide and produce complex fluid flow near the coverslip which makes fluid velocity estimates very approximate. Second, steady fluid flow is difficult to achieve for the lowest flow rates to calibrate forces below 70 pN. Third, the scatter in calibration of escape force is considerably greater than for the stage movement technique. The stage movement technique used in this work provides a more accurate escape force method to determine the velocity of the fluid from known stage velocity, thereby resolving some limitations of the fluid chamber method. The escape force generated over a range of laser powers is shown in Fig. 3-5. The incident laser power reported is measured prior to entering the objective lens. Due to losses from reflection and absorption, an incident laser power of 917 mW was observed for the maximum laser power setting of 1.5 W. The maximum stage velocity limits direct calibration at 400 mW of incident laser power. The escape force values for higher laser power is linearly extrapolated from the calibration data in Fig. 3-5. The maximum incident laser power, 917 mW, corresponds to an extrapolated escape force estimate of 193 ± 20 pN. The linear relationship between laser power and escape force is consistent with theoretical predictions [42] and empirical evidence [3]. Multiple calibration runs were performed at each power level before each set of experiments.

Specimen Preparation

Specimen preparation for testing healthy RBCs and *P. falciparum* parasitized RBCs involves the following steps. The general procedure for achieving the test configuration in Fig. 3-1 is described for tests reported in Chapters 4 and 5. The first step is a lancet finger prick to obtain a small sample of healthy fresh blood. *P. falciparum* parasitized RBCs were obtained from a microbiology laboratory[1]. The blood is centrifuged in PBS-BSA solution (0.1 mg/ml) three times at 1,000 rpm to wash and isolate RBCs. Silica beads are also centrifuged in PBS-BSA solution at 10,000 rpm three times. The RBCs and beads are mixed together and stored at 4°C for 1 h to allow for spontaneous and nonspecific adhesion of beads to RBCs. Prior to adding the RBC and bead solution into a test chamber, the coverslip is coated with BSA to prevent most adhesion between glass and the beads or

---

[1] The laboratory of Prof. K. S. W. Tan in the Department of Microbiology, Faculty of Medicine, National University of Singapore

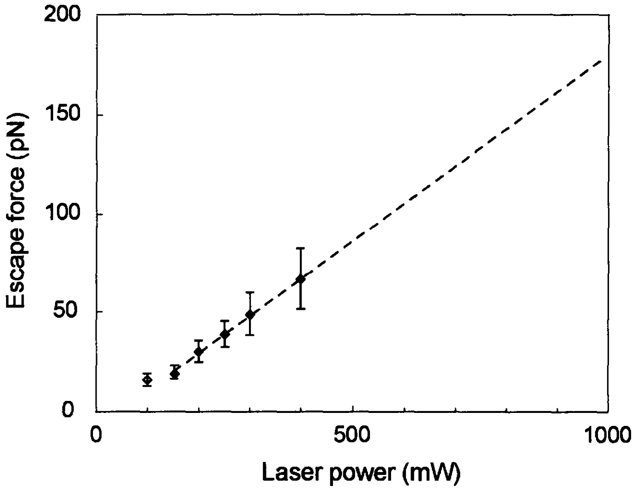

Figure 3-5: Force calibration plot showing the variation of trapping force with laser power for a 1.5 W diode pumped Nd:YAG laser source for a single optical trap system. Non-linear trends below 80 mW laser power are not used for extrapolation to higher laser powers.

RBCs. Some adhesion is necessary to achieve the test configuration illustrated in Figure 3-1. All experiments are completed within 1 h after RBCs are removed from storage at 4°C. Experiments are conducted when the correct test configuration (Fig. 3-1) is found. Correct bead arrangement can be confirmed by trapping the bead not attached to the slide. Because the optical trap is located above the slide surface and focal plane, a bead that is successfully trapped will appear out of focus, indicating that the bead is not adhered to the slide surface (see right bead in Fig. 3-1b). With this bead trapped, the stage can be translated to determine if the other bead (Fig. 3-1a) or part of the RBC membrane (Fig. 3-1b) is effectively adhered to the slide. Adherence to the slide is confirmed when the adhered bead or RBC membrane attachment point moves in a manner consistent with the stage and the RBC appears to be only in contact at the grip locations.

Uniaxial Tension Tests

A uniaxial tension test to determine the force–displacement response of a single RBC is performed by moving the coverslip relative to the trap to deform the cell. By stretching at different laser powers, corresponding to a range of calibrated escape forces, the force–displacement curve can be determined. All stretch tests are recorded digitally by a CCD

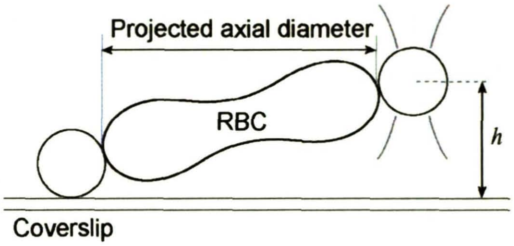

Figure 3-6: Optical images of stretch tests show the projected axial diameter because of a height difference between trapped and attached beads. With the trapped bead height known, the actual axial cell diameter can be calculated.

camera for image analysis of RBC deformation. For each stretch test, the axial diameter (in the direction of the uniaxial load) and transverse diameter (orthogonal to axial direction) of the cell are measured from the still-frame image when the trapped bead just escapes the trap. The calibration of laser power to escape force (Fig. 3-5) determines the force at this instant. From each point where the trapped bead escapes the trap, one data point on the force–displacement curve can be determined. Notice that the axial diameter is actually the projected axial diameter because of the height difference between the beads (Fig. 3-6). A correction factor for the actual axial diameter is made based on the known trapped bead height. A representative force–displacement curve for a healthy RBC determined the escape force method is plotted in Figure 3-7. The RBC membrane modulus is calculated from the force–displacement curve as described in Section 3.3.

Tests conducted at physiological temperatures (at 37°C and 41°C) were achieved by locally heating the test sample with resistive heaters. Optical tweezers tests were conducted at these temperatures after maintaining the test temperature for ten minutes. Two resistive heating pads attached to thin copper blocks were kept in thermal contact with the microslide to control the temperature at the sample. A thermocouple placed at the sample chamber was used to set and maintain the local local temperature to within ±1°C of the set temperature.

Viscoelastic Recovery Tests

Time dependent properties can be measured from the relaxation response of an RBC after the trapped bead escapes the trap. By measuring changes in axial and transverse

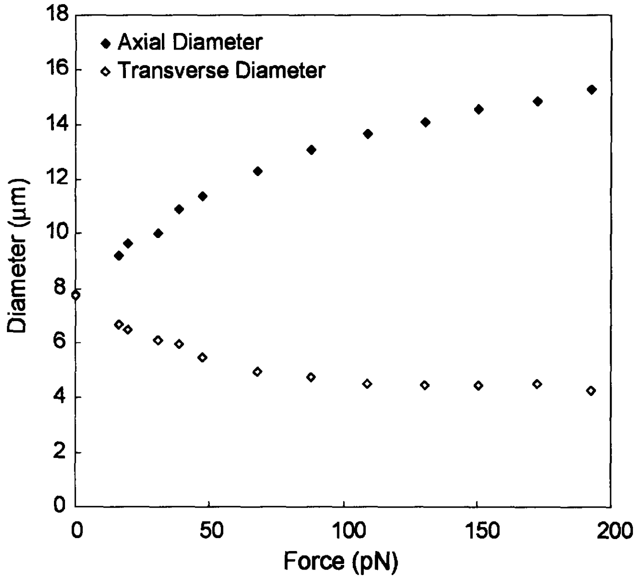

Figure 3-7: A representative force–displacement curve is plotted for a healthy RBC tested by the optical tweezers escape force method. The closed diamonds indicate the axial diameter and the open diamonds indicate the transverse diameter of the cell for increasing levels of applied uniaxial force.

diameters over time as the cell recovers its original shape, viscoelastic properties can be experimentally interrogated. Video images of the relaxation response of a stretched RBC upon release of trapping force post bead escape immediately after a uniaxial tension test can be used to infer the viscoelastic properties of the RBC membrane.

3.2.2 Trap Stiffness Method

The trap stiffness method optical tweezers instrument design, shown schematically in Figure 3-8, was also developed for experiments involving healthy and parasitized RBCs and is described further in detail *et al.* [43]. The instrument incorporates an inverted microscope (Nikon TE200) equipped with lasers for trapping (10 W, IPG Photonics) and position detection (970 nm, Avanex) that are collinearly guided into a 100× objective (1.40 NA, Nikon), which is based on a high-end optical trap instrument designed for single-molecule studies [44, 45]. The trapping laser path (red pathway in Fig. 3-8) passes through antireflection coated optics to minimize power losses before entering the objective. The trapping laser

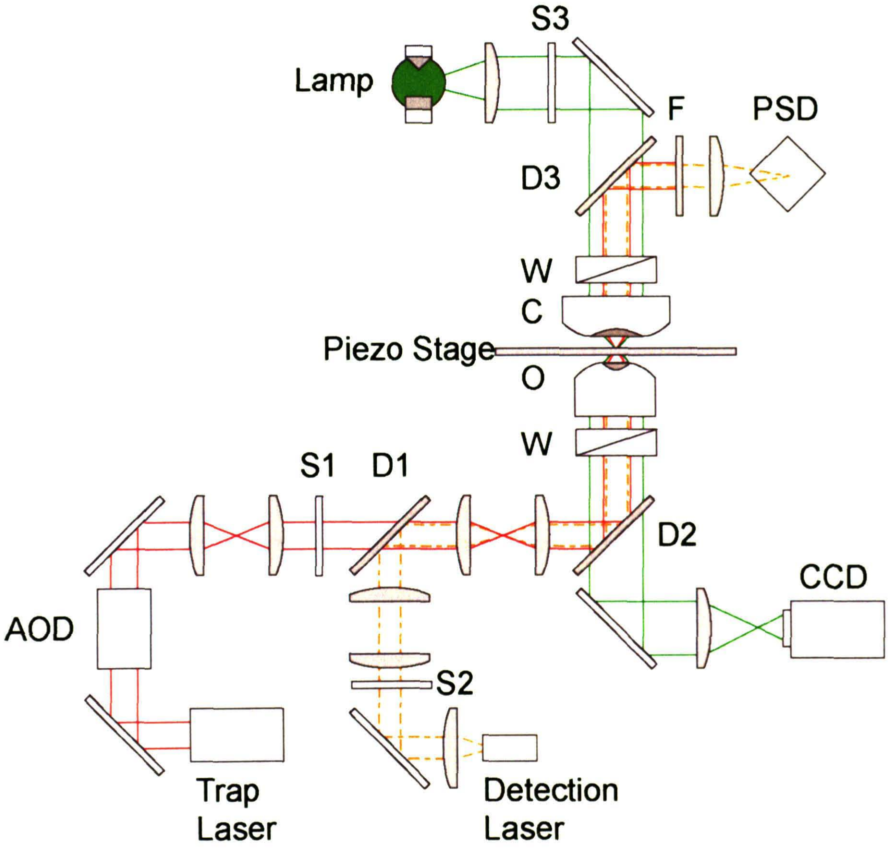

Figure 3-8: A diagram of the optical layout for the trap stiffness method optical tweezers instrument is shown. The trapping laser (red) and detection laser (dotted orange) are collinearly guided into the objective (O). The AOD automates laser trap positioning. The PSD detects the detection laser signal for measuring bead position. Experiments are recorded onto a CCD camera. The piezo stage is used for fine control of positioning the sample. Not all components are shown. (S, shutter; PBS, polarizing beam splitters; D, dichroic mirror; W, wollaston; C, condenser; F, filter)

path is guided into the illumination path (green pathway) by a low pass dichroic mirror (D2). Along the path, the trapping laser passes through acousto-optic deflectors (AODs) which are used to steer the trap in two dimensions in the focal plane and to regulate trap power. Computer control of AODs enables automation of the trap location and intensity. The high laser power and minimization of power losses due to optical absorption and reflection enable high forces to be achieved beyond the capabilities of the escape force method presented in Section 3.2.1. The laser-based position detection system incorporates a detection laser and PSD. The detection laser path (dotted orange pathway in Fig. 3-8) is guided into the trapping laser path by a high-pass dichroic mirror (D1). The signal of the detection laser is separated from the illumination pathway by another dichoic mirror (D3) and separated from the trapping laser signal by a filter (F). The detection laser path is ultimately focused onto a PSD, the signal being continuously acquired and used to determine the position of a trapped bead. Improved force calibration is achieved by using a separate position detection laser capable of detecting a trapped bead with position resolution <5nm. The piezo stage (Physik Instrumente), which is also computer controlled, is used for making fine displacements (position resolution <1nm) for RBC stretch tests. A CCD camera is used to image the specimen during experiments. Computer control of the AODs and piezo stage, along with acquisition of the PSD signal, adds automation to the instrument which was not available in previous RBC studies with optical tweezers [4, 28, 33, 41]. The particular advantages of this optical tweezers system are described here:

- High force capability: Forces up to and exceeding 600 pN can be achieved with the described set-up. This is roughly three times larger than the forces obtained by the escape force method described in Section 3.2.1 and in Mills *et al.* [4], and roughly ten times larger than forces reported in Hénon *et al.* [28] and Sleep *et al.* [33]. The high forces enable more of the nonlinear response of RBC in uniaxial tension to be studied.

- Increased force resolution: The scatter in forces calibrated by the present system compared to the escape force method described in Section 3.2.1 shows a reduction from around 20% to less than 5%. The increased force resolution leads to more accurate force–displacement data which, in turn, allows more subtle RBC membrane changes to be observed.

- Increased experimental throughput: The automation of experiments allows the force–displacement response and shear modulus measurement to be determined in real-time. Using the escape force method (Sec. 3.2.1) requires significant amounts of data analysis to extract the force–displacement curve. In addition, the continuous acquisition of force (via the laser-based position detection system) and displacements (via piezo stage control) permit a more continuous force–displacement curve to be obtained from a single RBC stretch test. In comparison, the escape force method requires multiple stretches to obtain discrete points that are used to construct the force–displacement curve.

- Study of time dependent properties: Automation and fine control over experimental parameters of force and displacement allow time-dependent property testing that was not possible with the escape force optical tweezers instrument. Tests involving stress relaxation, cyclic loading and strain-rate behavior are all easily implemented with the present optical tweezers trap stiffness instrument design.

The primary disadvantage of the trap stiffness is a significantly more complex optical layout compared to the escape force method.

Force calibration

Force calibration of the trap stiffness method optical tweezers instrument requires determination of the trap stiffness (reported in units of pN/nm) that corresponds to the slope of the applied force versus bead position plot within the linear region (Fig. 3-2). The bead displacement within the trap, measured by the position detection laser signal imaged on the PSD, is multiplied by the trap stiffness to continuously monitor the force exerted by the trap.

The trap stiffness is calculated by the Stokes' method, by moving the piezo stage at specified velocities and applying drag forces which can be calculated by Equations 3.1 and 3.2. The displacement of a trapped bead within the optical trap under an applied drag force is detected by the position detection signal. The slope of the bead position versus applied

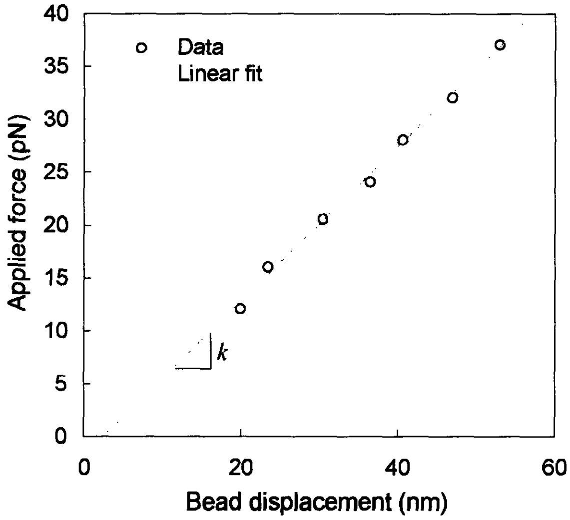

Figure 3-9: A force calibration by the trap stiffness method is plotted. Known drag forces are applied to a trapped bead by movement of the piezo stage at prescribed velocities. Forces are calculated by Stokes' law and appropriate corrections for wall effects (Faxen's law). The bead displacements within the trap are detected by the laser-based position detection system. The plot shows the linear relationship between applied force and trapped bead displacement for displacements close to the center of the trap. From the linear plot, the trap stiffness can be estimated. From this calibration, the trap stiffness is 0.73 pN/nm.

force yields the trap stiffness (Fig. 3-9)[2]. Tests were performed with an incident laser power entering the objective of 700 mW, which corresponded to a trap stiffness of 0.7 pN/nm for all 2 μm diameter beads with less than 5% error. Repeated force calibrations were performed before each set of experiments. Forces up to 350 pN were applied in force–displacement tests reported in Chapter 6.

With slight modifications to the present instrument, a variety of other stress states, other than simple uniaxial tension, are feasible. The AODs can be used to time share multiple traps or separate traps can be split off from the main trap pathway. Multiple traps can be used to optically trap multiple beads located on the membrane of an RBC and impose more complex states of stress (e.g. biaxial, shear loading).

Specimen preparation

For trap stiffness method tests, the following procedure is used. Fresh whole blood was obtained from a local source (Research Blood Components, Inc.). *P. falciparum* parasitized RBCs were cultured as described in detail in Chapter 6. Blood was centrifuged at 1,000 rpm in RPMI three times to wash and isolate RBCs. After the last centrifugation, the RBCs are suspended in PBS-BSA (0.1 mg/ml).

Polystyrene beads (2 μm diameter, streptavidin coated, Polysciences) were used in the trap stiffness method optical tweezers experiments. The index of refraction of polystyrene generates larger forces for a given laser power compared to silica. Also, the smaller bead diameter, 2 μm, used here compared to the 4 μm diameter beads used with the escape force method yield a smaller contact area with the RBC membrane that corresponds to more sensitive modulus measurement based on finite element simulations [25]. Polystyrene beads are coated with Concanavalin A (ConA, Sigma) to facilitate specific binding to the RBC membrane. Beads are first centrifuged three times in PBS-BSA at 10,000 rpm. ConA is added and the suspension is incubated at 4°C for 0.5 h. After, coated beads were centrifuged three more times in PBS-BSA at 10,000 rpm.

---

[2] The linear region extends up to 500 nm from the equilibrium trapped bead location under no applied forces.

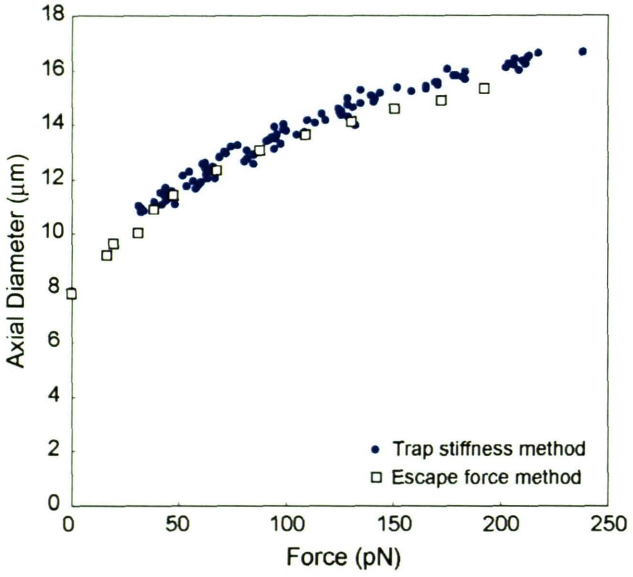

Figure 3-10: A representative axial force–displacement curve is plotted for a healthy RBC tested by the optical tweezers trap stiffness method (closed squares). For comparison, the results from a representative escape force method test (shown also in Fig. 3-7) are superimposed (open diamonds). Both techniques converge to produce a similar force–displacement response for healthy RBCs. In comparison, the data is more continuous and extends to higher forces than the escape force method.

The ConA coated beads are added to the RBC solution and placed in a specimen chamber. The coverslip is coated with BSA to limit bead and RBC adhesion, similar to the procedure in Section 3.2.1. The procedure for obtaining the test configuration in Figure 3-1b begins by trapping an unattached bead. After proper calibrations, the bead is brought into contact with an RBC that has a small part of the membrane attached to the coverslip so that the correct uniaxial test configuration can be achieved. The adhesion of ConA to the RBC membrane facilitates this adhesion in a few seconds. The correct configuration is confirmed by the same method described in Section 3.2.1.

Uniaxial Tension Tests

RBCs in the initial test configuration (Fig. 3-1) are deformed by the trap stiffness optical tweezers method to experimentally measure the single-cell force–displacement response. A piezo stage is used to move the coverslip by well-controlled displacements to apply deformations to the RBC. During deformation, the trapped bead position is continuously monitored by the detection-laser signal imaged onto the PSD. Automation of piezo stage movements and PSD signal acquisition allows capture of real-time force–displacement data. The axial force–displacement data from a representative RBC is plotted in Figure 3-10. Superimposed on this plot is axial data from Figure 3-7 from the escape force method. Both techniques produce consistent data for the mechanical response of an RBC in uniaxial tension. The advantages of the trap stiffness method are a more continuous force–displacement response to higher forces, greater accuracy, and higher experimental throughput.

Tests conducted at physiological temperatures used the same temperature system as described in Section 3.2.1.

3.3 Analysis of Experimental Data

The spectrin network which underlies the phospholipid bilayer of the human RBC is generally considered to impart shear resistance to the cell membrane because the bilayer itself has little resistance to shear deformation. As reviewed by Dao *et al.* [25], the effective cell membrane which comprises the phospholipid bilayer and the spectrin network is usually modeled as an incompressible solid [20, 21] where the membrane shear stress T_s (expressed in units of force per unit length) is related to the principal stretch ratios, λ_1 and λ_2, as

$$T_s = 2\mu\gamma_s = \frac{\mu}{2}(\lambda_1^2 - \lambda_2^2), \tag{3.3}$$

$$T_s = \frac{1}{2}(T_1 - T_2)\text{and}\gamma_s \equiv \frac{1}{2}(\varepsilon_1 - \varepsilon_2) = \frac{1}{4}(\lambda_1^2 - \lambda_2^2), \tag{3.4}$$

$$\lambda_1\lambda_2 = 1 \tag{3.5}$$

where T_1 and T_2 are the in-plane principal membrane stresses, ε_1 and ε_2 are the in-plane principal Greens strains of the membrane, μ is the membrane shear modulus (assumed to be constant and expressed in units of force per unit length) and γ_s is the shear strain. The assumption of a constant area for the cell membrane is usually invoked, as indicated by Equation 3.5. Other possible constitutive models can also be explored in the context of the deformation of RBCs. One such approach entails use of a hyperelastic effective material model for capturing the large deformation response of the membrane. Dao *et al.* [25] used the simplest first order formulation with a one-parameter Neo-Hookean form where the strain energy potential function [46] is of the form,

$$U = \frac{G_0}{2}(\lambda_1^2 + \lambda_2^2 + \lambda_3^2 - 3), \tag{3.6}$$

where the assumption of incompressibility (constant volume) is also invoked. Here G_0 is the initial value of bulk shear modulus, and λ_i $(i = 1 - 3)$ are the principal stretches. The incompressibility condition implies that $\lambda_1 \lambda_2 \lambda_3 = 1$. Further refinements to this approach are achieved by invoking a higher order formulation (a two-parameter Yeoh form [47] whereby

$$U = \frac{G_0}{2}(\lambda_1^2 + \lambda_2^2 + \lambda_3^2 - 3) + C_3(\lambda_1^2 + \lambda_2^2 + \lambda_3^2 - 3)^3. \tag{3.7}$$

In the current computations, we take values of the parameter C_3 to be those which best match experimental data ($C_3 = G_0/30$ in Chapter 4). The potential function U defines the nonlinear elastic stress-strain behavior. When the initial membrane thickness is h_0, the constitutive description of Equations 3.3, 3.4 and 3.5 results in the initial in-plane membrane shear modulus $\mu_0 = G_0 h_0$. Figure 3-11a schematically shows the uniaxial stress-strain response of such a neo-Hookean hyperelastic material, the membrane elasticity modulus typically decreases from its initially high value, μ_0, to a relatively smaller value, μ_l, at larger strains, before attaining a higher value, μ_f, again prior to final failure. The slope of the membrane shear stress (T_s) versus shear strain ($2\gamma_s$) is therefore initially a decreasing function of shear strain (Fig. 3-11b) and eventually transitions into a rapidly increasing function of shear strain (Fig. 3-11c). For the higher order response described by Equation 3.7, the first stage (μ_0) and the third stage (μ_f) will be the most important characteristic regions described. Specifically, μ_f (for the Yeoh description) is taken here at a relatively large stretch ratio of $\lambda_1 = 2$ under direct uniaxial tension. The neo-Hookean rubber elasticity model for the membrane entails two material parameters: the initial shear modulus

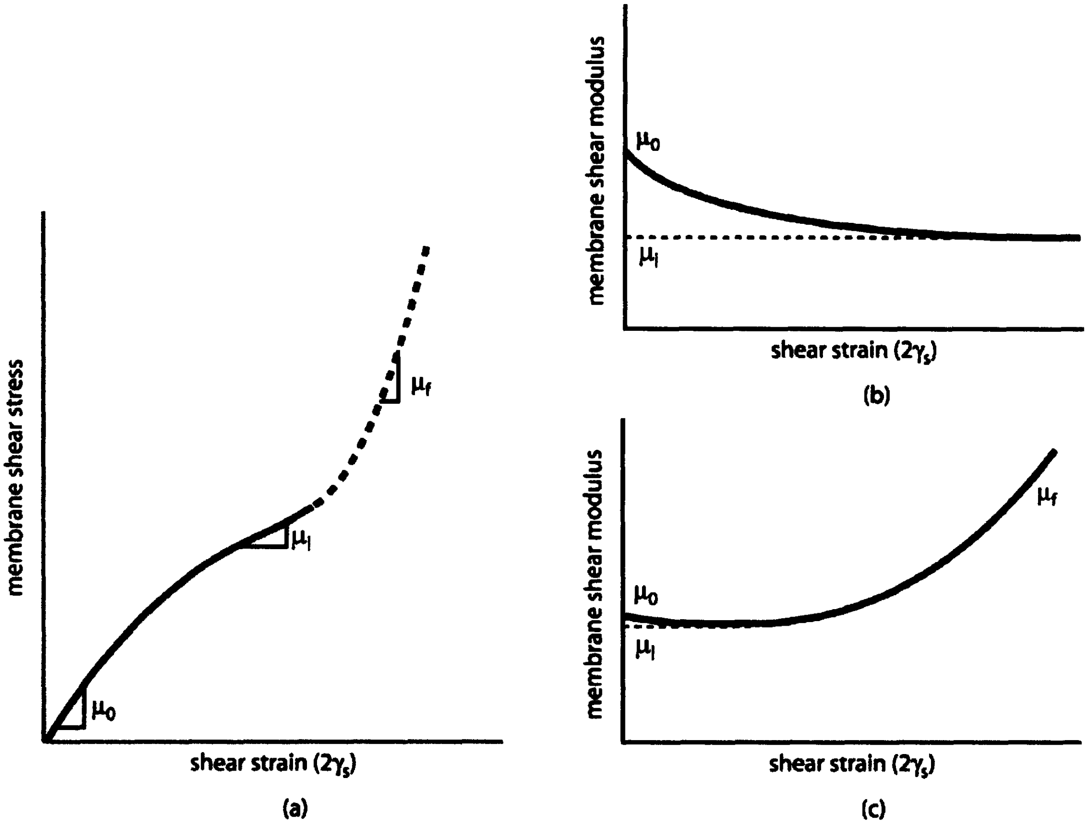

Figure 3-11: Schematic illustration of the hyperelastic constitutive response used in some of the computational simulations. (a) Uniaxial stress-strain response. (b) The variation of the membrane shear modulus with the progression of deformation of the first order hyperelasticity model, where strains are representative of the large deformation response achieved in the present optical tweezers experiments. (c) The variation of the membrane shear modulus with respect to shear strain of a higher order hyperelastic model.

μ_0 and the second stage, large deformation modulus μ_l. In the current first order model, selection of one value of the two parameters also determines the other; while introducing higher order term C_3 results in independent variations of μ_0 and μ_f (Fig. 3-11c). Selection of these parameters, which optimizes the agreement between computational predictions and experimental results, has been systematically explored, and reported in Mills *et al.* [4] and in Dao *et al.* [25].

When the constant membrane area constraint, i.e. $\lambda_1 \lambda_2 = 1$ (where $\lambda_3 = 1$), is incorporated into Equation 3.6, the constitutive description of Equation 3.6 is equivalent to that of Equations 3.3, 3.4 and 3.5. With this additional constraint, the in–plane membrane shear modulus stays at a constant value of $\mu = G_0 h_0$ throughout the entire deformation history [25].

Calculations of membrane shear modulus based on the classical assumption of incompressibility and constant membrane area ($\lambda_1\lambda_2 = 1$, $\lambda_3 = 1$) are exactly 75% of the value calculated when the current assumption of constant membrane volume ($\lambda_1\lambda_2\lambda_3 = 1$) is invoked, which relaxes the thickness constraint of $\lambda_3 = 1$. The classical assumption of constant membrane area was based on the area conserving lipid bilayer to which the spectrin network is attached [20]. However, fluorescence-imaged micropipette aspiration experiments reveals that the density of spectrin and other cytoskeletal proteins experience a steep gradient along the aspirated membrane length, which was not seen with the lipid bilayer [48]. These experiments indicate that the constant area assumption valid for the lipid bilayer can not be directly extended to the spectrin network. The global area of the RBC is preserved by the lipid bilayer, but the local spectrin network density can change substantially. For the constant membrane area assumption, the molecular nature of the cytoskeleton in the direction perpendicular to the membrane is not captured by allowing for λ_3 to be values other than 1. The difference between extracted shear modulus values based on constant area and constant volume constraints is 25% (the constant volume assumption yielding a relatively higher shear modulus) [49], with the actual response likely in between these two idealizations. The constant difference allows results based on either assumption to be easily compared. All shear modulus calculations in this thesis are presented based on constant membrane volume. (Literature data based on constant area assumptions have been converted to an equivalent membrane shear modulus constant volume value.)

While the foregoing analytical descriptions for the thin shell employ a single material property, i.e., the membrane shear modulus, more comprehensive analyses involving computational simulations of cell deformation invoke another material parameter in addition to the in-plane shear modulus, μ: the bending modulus, B. It is generally known that the contribution to the uniaxial tensile elastic deformation of the red blood cell from the bending modulus is much less than that from the shear modulus. Therefore, a typical (fixed) value of $B = 2 \times 10^{19}$ $\mathrm{N \cdot m}$ is assumed in all the computations unless specified otherwise. We match the computational simulations with experimentally observed evolution of axial and transverse cell diameters at different forces imposed by the optical tweezers, and then extract shear modulus on the basis of the foregoing constitutive assumptions. Computational simulations of large deformation stretching of the cell by optical tweezers were performed using three-dimensional finite element analysis of the biconcave red blood cell containing the cytosol in the interior. Because of symmetry in the optical tweezers loading geometry, it suffices to simulate one half of the cell contacted by a bead. Symmetric boundary conditions with 12,000 three-dimensional shell elements were employed in the simulations using the general purpose finite element program, ABAQUS [50]. Full details of the computations can be found in Dao *et al.* [25].

The implementation of a continuum description to model the RBC for extracting the RBC membrane shear modulus by finite element modeling is validated at the molecular level by molecular dynamics simulations [49, 51]. A three-dimensional computational formulation of all spectrin network molecules based on a worm–like chain model was shown to be consistent with the predictions of continuum level finite element modeling and optical tweezers experiments.

Sample sizes are noted for all tests conducted. For many samples, ten or fewer tests were conducted. Significant differences in results between two sample sets were performed by p-value statistics that account for the small sample sizes. Bars are shown for all data sets to indicate the amount of scatter observed in measurements. Literature values for healthy RBC shear modulus vary by over 50%, from 4 to 10 μN/m [20, 26, 30, 31]. Although it is not clear how much of the scatter is due to variations in different blood samples and how much is from experimental considerations, some scatter in results is expected.

Chapter 4

Healthy Red Blood Cell Deformability

4.1 Introduction

The RBC membrane permits large cell deformations required for normal circulation through small capillaries and spleen sinusoids. Measurement of the RBC membrane shear modulus has been performed primarily by micropipette aspiration experiments that deform only a portion of the RBC membrane [20, 26, 30, 31]. In this chapter, the first large-deformation, single-cell mechanical tests of RBCs under a well-defined uniaxial loading geometry is presented based on escape force method optical tweezers experiments. The elastic shear modulus and viscoelastic properties are measured and compared to literature data generated by the micropipette aspiration technique. The results presented in this section, except where noted otherwise, were originally published in Mills *et al.* [4].

4.2 Results and Discussion

Deformability at Standard Test Temperature

Similar to nearly all previous studies on RBC membrane shear modulus [20, 26, 30,

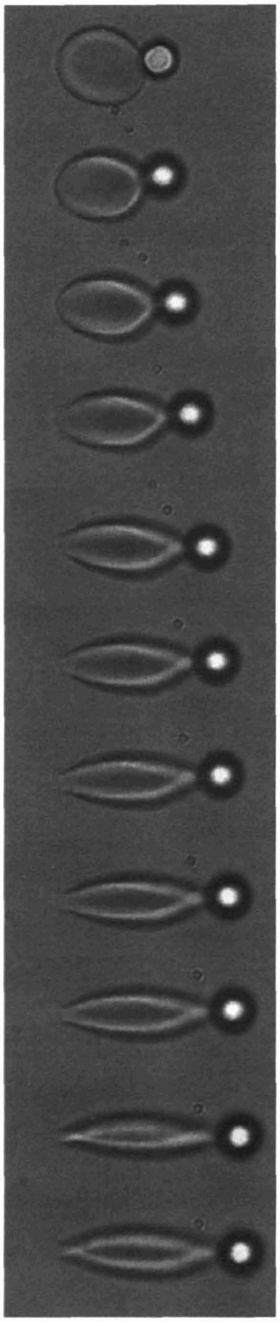

Figure 4-1: A representative RBC optical tweezers test. The microscopy images show a RBC under incrementally applied forces of (from top to bottom) 0, 20, 38, 48, 68, 88, 109, 130, 151, 173 and 193 pN during an optical tweezers experiment. As the applied force increase, the axial diameter (in the direction of uniaxial tension) increases and the transverse diameter (perpendicular to the axial diameter) decreases. Large geometrical changes to the RBC are observed for the cell to accommodate large deformations. Scale: The silica bead is 4.12 μm in diameter and the initial RBC diameter under no applied force is 8.4 μm.

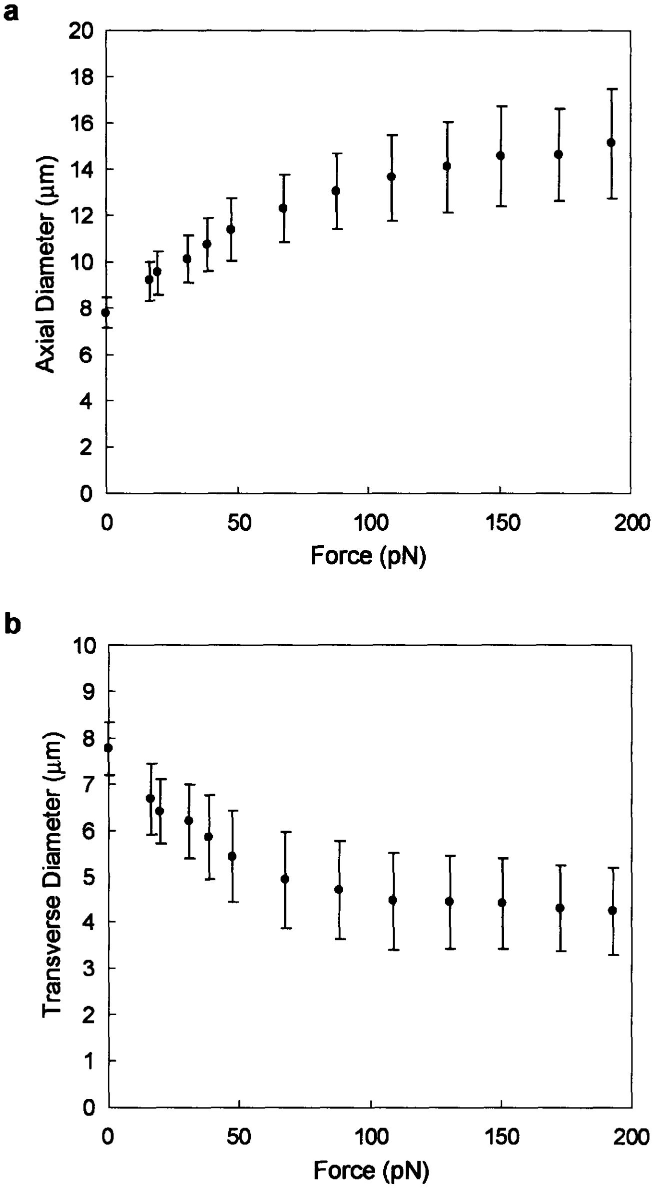

Figure 4-2: Force-displacement data from optical tweezers tests on single RBCs. The average response from experimental data on sixteen healthy RBCs tested in uniaxial tension with scatter bars indicating the range of responses observed for **(a)** axial and **b** transverse cell diameter change. Significant increase in axial diameter and decrease in transverse diameter (up to 2-fold) indicates the ability of the RBC to accomodate large deformations. When the applied load is removed, large deformations are fully recovered, indicating the elastic nature of the RBC membrane.

31], experiments presented in this section were conducted at laboratory temperature (21°C). Figure 4-1 shows microscopy images of RBC deformations from one representative uniaxial tension test. The capacity for the RBC to accommodate large deformations is evident from these images. When the load is removed, the RBC recovers its original shape, indicating the elastic nature of the membrane. The force-displacement curves obtained by optical tweezers escape force method testing of sixteen RBCs in uniaxial tension incrementally from 0 to 190 pN are plotted in Figure 4-2. As applied force increases, the RBC axial diameter increases (Fig. 4-2a) and the transverse diameter decreases (Fig. 4-2b).

The RBC membrane shear modulus is extracted from experimental force-displacement data via finite element computations (Sec. 3.3). Figure 4-3 plots the average experimentally measured RBC force-displacement response with scatter bars representing the range of responses observed in the sixteen samples shown individually in Figure 4-2. Superimposed on Figure 4-3 are finite element predicted changes in axial and transverse diameters of a RBC using the higher order Yeoh model in Equation 3.7 for three different shear modulus values, $\mu_0 = 5.3, 7.3$ and 11.3 μN/m (with $\mu_f = 13.9, 19.2$ and 29.6 μN/m, respectively). For simulations, the initial RBC diameter was set to 7.5 μm and the contact region between the bead and RBC, d_C, was set to 2 μm. Simulations are seen to accurately capture experimental trends over the entire range of data. (Analysis based on a neo-Hookean model (Eq. 3.6) captures experimental trends over the range of $0 - 88$ pN well, while they deviate towards a softer response beyond 88 pN load.) From analysis of optical tweezers force-displacement data, the RBC membrane shear modulus is in the range of $5.3 - 11.3$ μN/m, with an average of 7.3 μN/m. In other series of tests conducted at laboratory temperature (21°C to 25°C), nominal healthy RBC membrane shear modulus values of 8.5 μN/m (Fig. 4-5) and 5.3 μN/m (Sec. 5.2) were measured. If the classical assumption of area conservation is enforced ($\lambda_1 \cdot \lambda_2 = 1$), the calculated shear modulus values are decreased by 25%. Based on all sets of experiments on healthy RBCs, the nominal shear modulus values are recalculated to be 4.0, 5.5 and 6.3 μN/m. These values are comparable to the range of $4 - 10$ μN/m reported in the literature based principally on micropipette aspiration experiments and invoking the assumption of area conservation in analyses [20, 26, 30, 31]. The results presented in this section are different than those derived from earlier optical tweezers studies of Hénon *et al.* [28] and Sleep *et al.* [33] for small elastic deformation, indi-

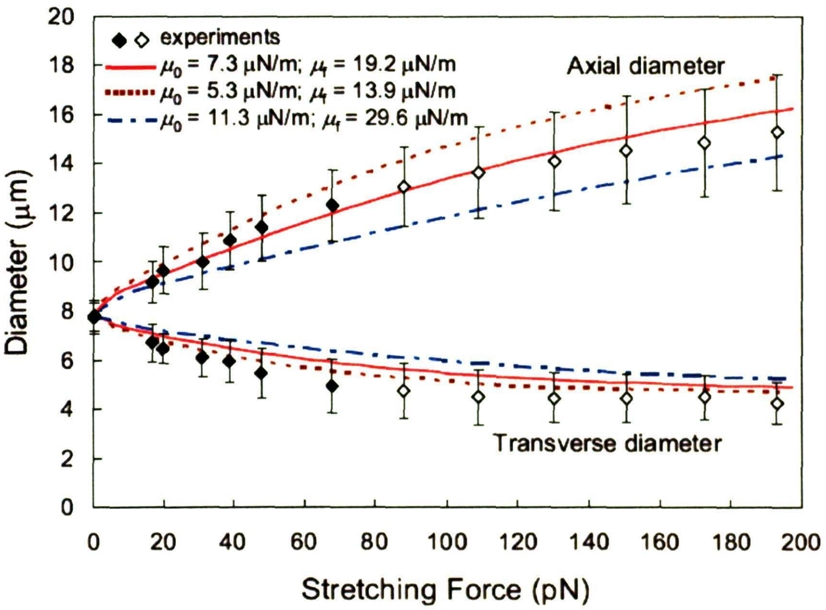

Figure 4-3: Experimental results and computational predictions for RBC force-displacement response. The average experimental force-displacement curve (data points) and associated scatter bars are based on the sixteen optical tweezers RBC tests. To determine the healthy RBC membrane shear modulus from experiments, computational simulations are matched to the experimental data. The three computational force-displacement curves shown are generated by varying the RBC membrane shear modulus $\mu_0 = 5.3, 7.3$ and 11.3 μN/m, and $\mu_f = 13.9, 19.2$ and 29.6 μN/m, respectively, invoking a higher order hyperelastic constitutive response, Equation 3.7, which assumes constant membrane volume (not constant area). The closed data points (black diamonds) represent the portion of the force–displacement curve that reflect the initial shear modulus (μ_0), whereas the open points (white diamonds) represent the large deformation nonlinear response which the higher order hyperelastic term (μ_f) captures. From experimental and computational analysis, the RBC membrane shear modulus is measured to be within the range of $5.3 - 11.3$ μN/m, with an average of 7.3 μN/m. This figure is adapted from Mills *et al.* [4]

cating that differences in calibration as well data analysis methods may have influenced the elastic properties extracted from these optical tweezers experiments. Modeling the RBC as a two-dimensional planar disc [28] and neglecting the effect of large contact regions between the RBC and bead [33] could account for the disparity in results between previous optical tweezers experiments [28, 33] and accepted values from micropipette aspiration techniques.

Figure 4-4 shows that observed shape changes are matched by computational simulations when $\mu_0 = 7.3$ μN/m (with $\mu_f = 19.2$ μN/m) using the higher order hyperelastic Yeoh model described by Equation 3.7. The left column in the figure is a sequence of optical images revealing the large deformation response of a representative RBC at the indicated applied force. At 193 pN, the axial diameter of the cell increases by 50% and the transverse diameter is reduced by more than 40%. The middle column shows contours of constant maximum principal strain at corresponding stretching forces; strains near sites of contact between the cell and the beads can reach values of approximately 100% at an applied force of 193 pN. The right column shows a cut-away view of the computed full three-dimensional shape of a RBC at the indicated imposed force. The structural folding observed at large strains appears to contribute significantly towards the shrinking in the transverse direction. Evidence of such folding is also seen experimentally, as for example in the images at higher force in Figure 4-1 and the lower images in the left column of Figure 4-4.

Deformability at Physiological Temperatures

The value of RBC membrane shear modulus at physiologically relevant temperatures has not been extensively studied in the literature. The optical tweezers escape force method used in the preceding section to measure the shear modulus under laboratory temperature (21°C) was used to measure RBC force-displacement response at physiological temperatures, 37°C (normal) and 41°C (febrile)[1]. The results of optical tweezers tests on healthy RBCs at 21°C, 37°C and 41°C is given in Figure 4-5. The RBC membrane shear modulus is shown to remain stable over the range of tested temperatures. Within the level of normal experimental scatter, the shear modulus of the healthy RBC membrane is relatively unaffected

---

[1] The procedure for calculating the shear modulus reported in this section is slightly different than described in the methods in Section 3.2.1. Instead of averaging the force-displacement response of all tests at a given temperature, each RBC force-displacement response was analyzed by an analytical solution based on closed-form scaling functions from extensive parametric simulations using FEM. This analysis method is described in Section 3.3

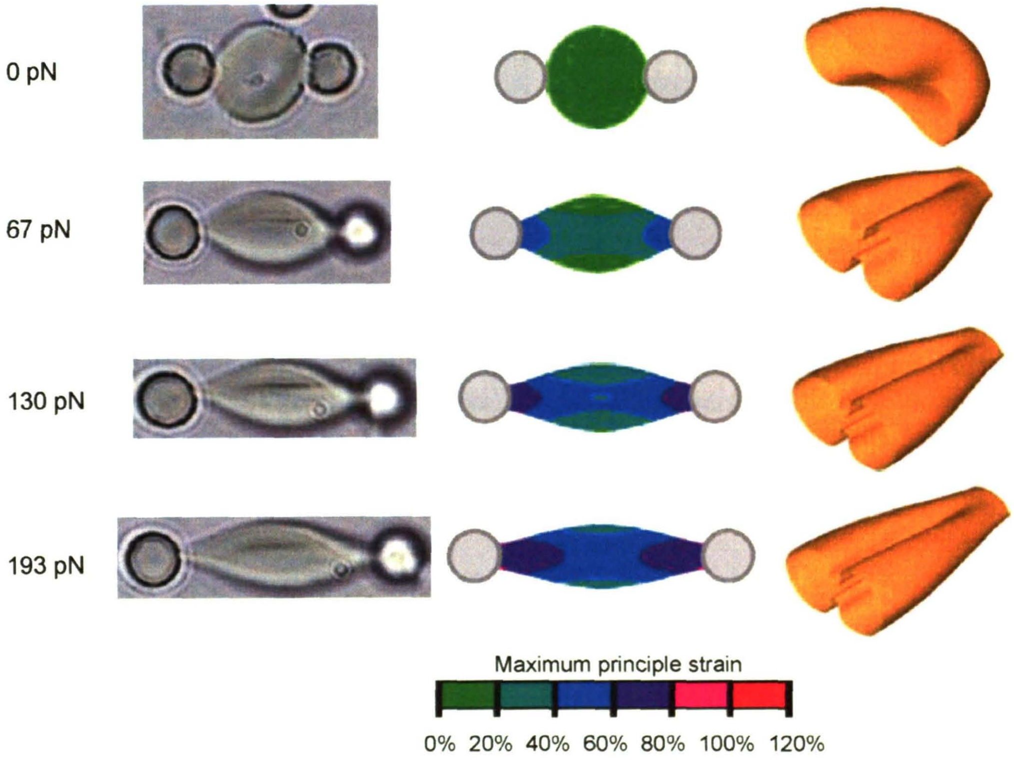

Figure 4-4: Images of an RBC and finite element RBC model under uniaxial tension at 0, 67, 130 and 193 pN. Optical images (**left column**) are obtained from experimental video photography. A top view (**center column**) and half model 3D view (**right column**) correspond to large deformation computational simulation of the biconcave RBC with $\mu_0 = 7.3\ \mu$N/m, $\mu_f = 19.2\ \mu$N/m). The middle column shows a plan view of the stretched biconcave cell undergoing large deformation at the forces indicated. The predicted shape changes are in agreement with experimental observations. The color contours in the middle column represent spatial variation of constant maximum principal strain. The right column shows one half of the full three-dimensional shape of the cell at different imposed forces. This figure is adapted from Mills *et al.* [4]. Scale: The silica bead is 4.12 μm in diameter and the RBC under no applied force has a diameter of 8.1 μm.

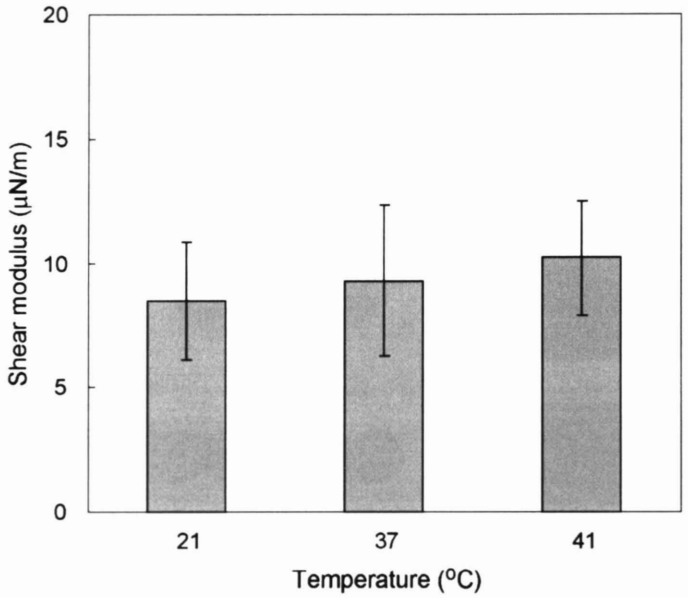

Figure 4-5: RBC membrane shear modulus measured by optical tweezers tests at laboratory (21°C), normal body (37°C) and febrile (41°C) temperatures. The shear modulus value was goung to be relatively unaffected by temperature over within the range of temperatures investigated.

by a change in temperature. Based on the present data and data reported by Waugh it et al. [5, 52] between 16°C and 41°C, there does not appear to be a temperature trend (Fig. 4-6. (Waugh [5] does predict some temperature trend from data plotted in Figure 4-6 that appears weighted by the values obtained at the extremes.) By combining the current results with data from Waugh [5] from 16°C to 41°C, the results are consistent and show no effect over a physiologically relevant temperature range.

Red Blood Cell Viscoelastic Recovery

Hochmuth *et al.* [53] estimated the recovery characteristic time t_c of the RBC to be

$$\frac{(\lambda_1^2 - 1)(\lambda_{1,\mathrm{max}}^2 + 1)}{(\lambda_1^2 + 1)(\lambda_{1,\mathrm{max}}^2 - 1)} = \exp(-\frac{t}{t_c}) \tag{4.1}$$

where λ_1, max is the initial (maximum) value of the stretch ratio of the red cell and the characteristic time for relaxation is given by

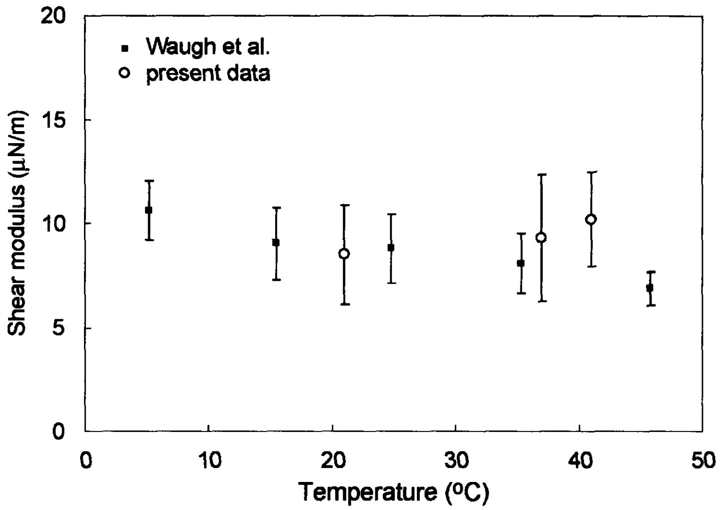

Figure 4-6: RBC membrane shear modulus measured at various temperatures by micropipette aspiration [5] and in the present optical tweezers study (not previously published). Over the range of temperatures from laboratory to physiological conditions, both techniques show relatively constant RBC membrane shear modulus measurements.

$$t_c = \frac{\eta}{\mu} \tag{4.2}$$

where η is the coefficient of surface viscosity of the cell membrane, and μ is the in-plane shear modulus of the membrane.

Figure 4-7 shows the corresponding best fit to the experimental data on relaxation using Equation 4.1. Based on relaxation data from eight different experiments, the characteristic time is estimated to be $t_c = 0.19 \pm 0.06$ s. It is noted here that micropipette aspiration experiments have led to estimates of characteristic time of relaxation from large deformation of the red blood cell to be in the range $0.10 - 0.30$ s [53, 54], which agrees with the current findings. With membrane shear modulus values taken to be $5.3 - 11.3$ μN/m, the corresponding membrane viscosity, η, calculated from Equation 4.2 and Figure 4-7 is 0.3 to 2.8 (μN/m) $\cdot$ s, which compares well with the literature values of 0.6 to 2.7 (μN/m) $\cdot$ s found using micropipette experiments [53].

To evaluate the contribution of membrane viscosity, three-dimensional computational simulations of the loading response are performed by incorporating the viscoelastic

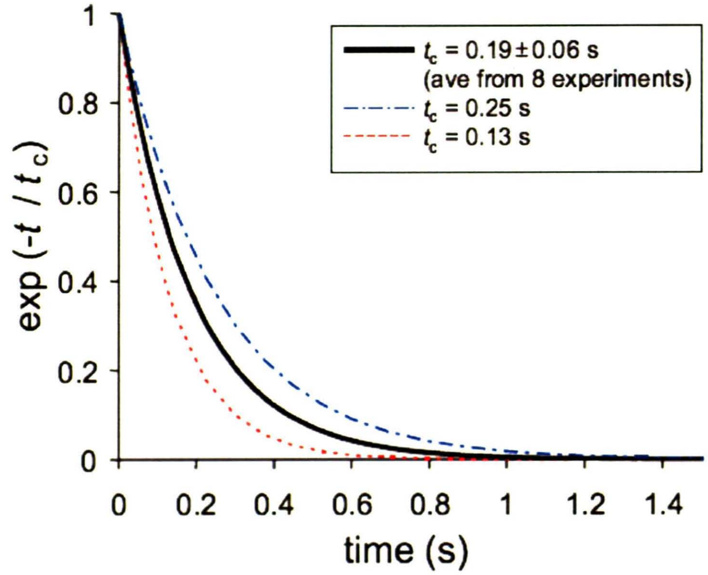

Figure 4-7: Best fits to the experimental relaxation data are plotted. Using relaxation data from eight different experiments, the characteristic time of relaxation was estimated to be $t_c = 0.19 \pm 0.06$ s using Eq. 4.2. This figure is adapted from Mills *et al.* [4]

term to the constitutive behavior of the cell membrane by modifying Equations 3.3, 3.4 and 3.5 as [20, 25],

$$T_s = \frac{\mu}{2}(\lambda_1^2 - \lambda_1^{-2}) + 2\eta \frac{\partial \ln \lambda_1}{\partial t} \tag{4.3}$$

where t is time, and t_c is the characteristic time for relaxation. For $t_c = 0.19$ s and an estimated stretch rate of $\dot{\lambda}_1 = 0.3\ \mathrm{s}^{-1}$, the error caused by ignoring membrane viscosity during the loading stage is found to be negligibly small.

A new study on viscoelastic response of RBCs based on magnetic twisting cytometry points out that the viscoelastic response over a large frequency range follows a power law decay rather than an exponential decay [55]. Consequently, the characteristic times of constants for shape recovery determined by micropipette aspiration and optical tweezers may be strongly influenced by the limited range of temporal duration of experiments where recovery of shape is dominated by membrane shear. Thus, the measured characteristic times from these techniques may not completely reflect the viscoelastic behavior because they are fit to an exponential over a limited temporal range [55]. Nevertheless, the measured relaxation response by micropipette aspiration and optical tweezers suggests a short time is required for RBCs to recover their original shape after sustaining large deformations. Furthermore, agreement between the standard micropipette aspiration technique validates the use of optical tweezers for studying RBC shape recovery.

4.3 Summary

The shear modulus of the RBC membrane was measured by conducting uniaxial force–displacement tests by an escape force optical tweezers method coupled with three-dimensional finite element model simulations incorporating specific test parameters. The shear modulus of the RBC membrane at laboratory temperature is measured to be in the range of $5.3-11.3$ μN/m, with an average of 7.3 μN/m. The nominal values of membrane shear modulus from three seperate sets of tests on healthy RBCs were 7.3 (Fig. 4-3), 8.5 (Fig. 4-5) and 5.3 (Sec. 5.2) μN/m. This range of shear modulus values is in agreement with accepted values based on micropipette aspiration experiments [20, 26, 30, 31]. The measured shear modulus at physiological temperatures (37°C and 41°C) was comparable to results from tests at laboratory temperature. Data presented in this chapter and from Waugh [5] between 16°C and 41°C clearly show that the RBC membrane shear modulus is insensitive over that temperature range. The characteristic time of relaxation by monitoring the recovery of RBC shape after large deformations applied by optical tweezers was measured to be $t_c = 0.19 \pm 0.06$ s, which also is in agreement with values derived from micropipette aspiration experiments [53, 54].

The good agreement between the results from the optical tweezers approach presented in this chapter and that from previous micropipette aspiration experiments [20, 26, 30, 31] demonstrates that both methods are capable of accurately determining the deformability characteristics of RBC membranes. A primary advantage of the optical tweezers method is that it captures the deformation of an entire RBC, whereas the micropipette aspiration method only deforms a localized region of the membrane. In addition, frictional forces that exist between a RBC and micropipette (e.g. *P. falciparum* parasitized RBCs that exhibit strong adhesion properties not seen in healthy RBCs) that can complicate analysis are not a limitation when using the present optical tweezers method.

Chapter 5

P. falciparum Parasitized Red Blood Cell Deformability

5.1 Introduction

An investigation of altered deformability of *P. falciparum* parasitized RBCs (pRBCs) that causes dramatic changes to blood circulation is presented in this chapter. Intra–erythrocytic development of *P. falciparum* is known to cause pRBCs to display decreased deformability and novel cytoadhesion properties that can contribute to sequestration of pRBCs in the microvasculature [2]. Sequestration can lead to compromised blood flow and life-threatening complications in severe cases of malaria [2]. While pRBC cytoadhesion has been extensively studied [2], pRBC deformability changes have been limited to the studies discussed in Chapter 2 [6, 7, 39, 40, 56]. Previously attempts by micropipette aspiration [7, 39] and laminar shear flow [8] experiments have not been able to measure the *P. falciparum* pRBC membrane shear modulus over the entire range of parasite erythrocytic developmental stages due to experimental limitations. Additionally, these techniques can not capture the single–cell force–displacement response.

Optical tweezers offer a technique to measure the pRBC membrane shear modulus over all intra–erythrocytic developmental stages of *P. falciparum* without the experimental limitations of previous techniques. Use of optical tweezers to measure the single healthy

RBC force–displacement response and membrane shear modulus was demonstrated in Chapter 4. In this chapter, for the first time, continuous force-displacement curves from *in vitro* deformation of RBCs and pRBCs at all intra–erythrocytic developmental parasite stages are generated with optical tweezers. By integrating this information with finding from related studies [7, 38] on protein-specific contributions to RBC elasticity, we seek to establish connections among protein structure, mechanical properties of pRBCs and possible effects on disease progression. Results presented in this chapter were originally published in Suresh *et al.* [6] and Mills *et al.* [9].

5.2 Results and Discussion

Force-displacement curves for *P. falciparum* parasitized RBCs

P. falciparum pRBCs were studied at each intra–erythrocytic developmental parasite stage: ring (0−24 h post parasite invasion); trophozoite (0−36 h); and schizont stage (36−48 h)[1]. Two control conditions were tested: healthy and parasite-free RBCs. Parasite–free RBCs were present in *P. falciparum* cultures, but had not been invaded by a parasite; healthy RBCs were not exposed to parasite cultures.

The left column of Figure 5-1 shows optical images of pRBCs at each intra–erythrocytic developmental stage[2] and the two control conditions prior to *in vitro* testing by optical tweezers at 25°C. Similar to previous work on healthy RBC membrane shear modulus measurements, nearly all studies on pRBCs were also conducted at laboratory temperature. The parasite is visible inside the three pRBCs. Also shown in this figure are the deformed

---

[1] Experiments involved *in vitro* culturing of *P. falciparum* strains 3D7 [57] and Gombak A [58] using methods described previously [59] with appropriate modifications [60]. Cultures were grown at 5% hematocrit in 25 ml tissue culture flasks in a complete medium that consisted of RPMI 1640 supplemented with 4.2 ml/100ml 5.0% NaHCO3 and 0.5% w/v albumax (Gibco-BRL). Cultures were gassed with 3% O2, 5%CO_2 and 92% N_2, and incubated at 37°C in complete medium. Culturing was performed by the laboratory of Prof. Kevin S. W. Tan at the National University of Singapore.

Compared to the experimental methods employed for the optical tweezers stretching of healthy RBCs [4] described in Section 3.2.1, the procedure for storage at 4°C was omitted for trophozoite and schizont stage pRBCs described here so as to reduce possible cell damage. The adhesion of silica beads to pRBCs at the trophozoite and schizont stages was naturally enhanced because of the increased adhesion of late stage pRBCs.

[2] The transition of pRBCs to more mature stages occurs continuously, which often makes identification of exact intra-erythrocytic development stage difficult. For results reported in this chapter, pRBCs only within one well-defined parasite development stage are included.

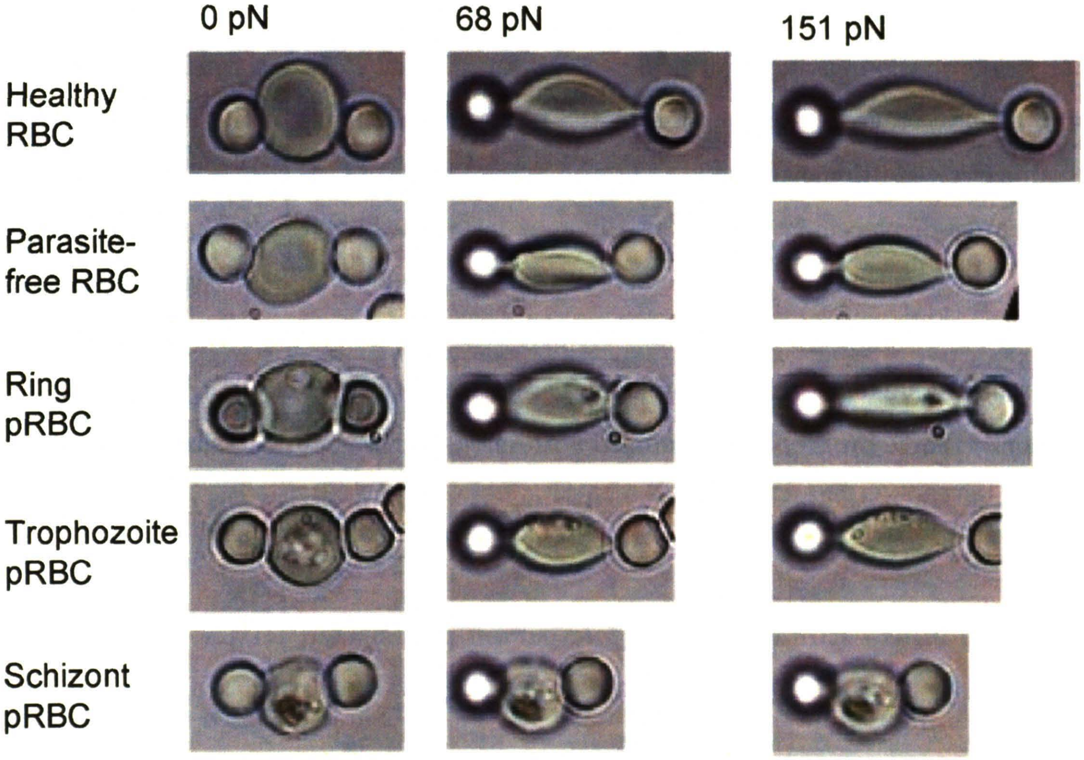

Figure 5-1: Representative optical images of RBCs and pRBCs at indicated intra–erythrocytic parasite developmental stages (**left column**) under no applied force, (**center column**) 68 ± 12 pN and (**right column**) 151 ± 20 pN of uniaxial applied force. The images of the healthy RBC illustrate the large strains that the RBC membrane can withstand. The deformability of healthy RBCs was presented in detail in Chapter 4. Deformability is progressively decreased from the ring stage to the trophozoite stage to the schizont stage in pRBCs. Parasite–free RBCs were found to be somewhat less deformable than healthy RBCs not exposed to *P. falciparum* cultures. This figure was adapted from Suresh *et al.* [6]. Scale: Silica beads are 4.12 μm in diameter.

shapes of the cells at applied forces of 68 and 151 pN. While ring and trophozoite stage pRBCs exhibit some noticeable deformability at both load levels, little deformation is seen in the schizont stage pRBC. The deformation for parasite–free RBCs is slightly smaller than that for healthy RBCs. At a fixed stretching force, the deformability of the pRBCs is significantly reduced compared to that of the two control conditions.

Figure 5-2a shows the increase in the axial diameter of RBCs and pRBCs in response to large deformation testing by optical tweezers for different *P. falciparum* intra–erythrocytic developmental stages. The decrease in the transverse diameter of the RBC or pRBC for the same five conditions is plotted in Figure 5-2b. The data in Figure 5-2 thus provide continuous force-displacement curves for different intra–erythrocytic developmental stages of pRBCs. The experimental data (discrete data with error bars) indicate significant stiffening of pRBCs as a function of parasite maturation from the ring stage to the trophozoite stage to the schizont stage; the increase in axial diameter and the decrease in transverse diameter with applied force progressively diminish with intra–erythrocytic parasite development. In the schizont stage, the pRBC has very little deformability in either the axial or transverse directions.

Elastic modulus estimates for *P. falciparum* parasitized RBCs

Superimposed on experimental data in Figure 5-2 are simulated variations of axial and transverse diameters of RBCs and pRBCs using a three-dimensional hyperelastic constitutive model incorporated into a finite element code. From the matching of computational results, shown by the dotted lines in Figure 5-2 for the different parasite erythrocytic developmental stages, with experimental data, the average shear modulus of each test condition RBC and pRBC was extracted. The best measure of RBC or pRBC membrane deformability is the shear modulus, which is related to the slope of the force–displacement curve up to around 80 pN. Figure 5-3 shows the median value (marked by a small vertical line) and range of shear modulus values corresponding to the results of pRBC and control RBC conditions, from the optical tweezers experiments and computational simulations. These values are based on repeat experiments conducted on 7 healthy RBC, 8 parasite–free RBC, 5 ring stage pRBC, 5 trophozoite stage pRBC, and 23 schizont stage pRBC samples. Also shown in this figure are the shear modulus values estimated from other independent exper-

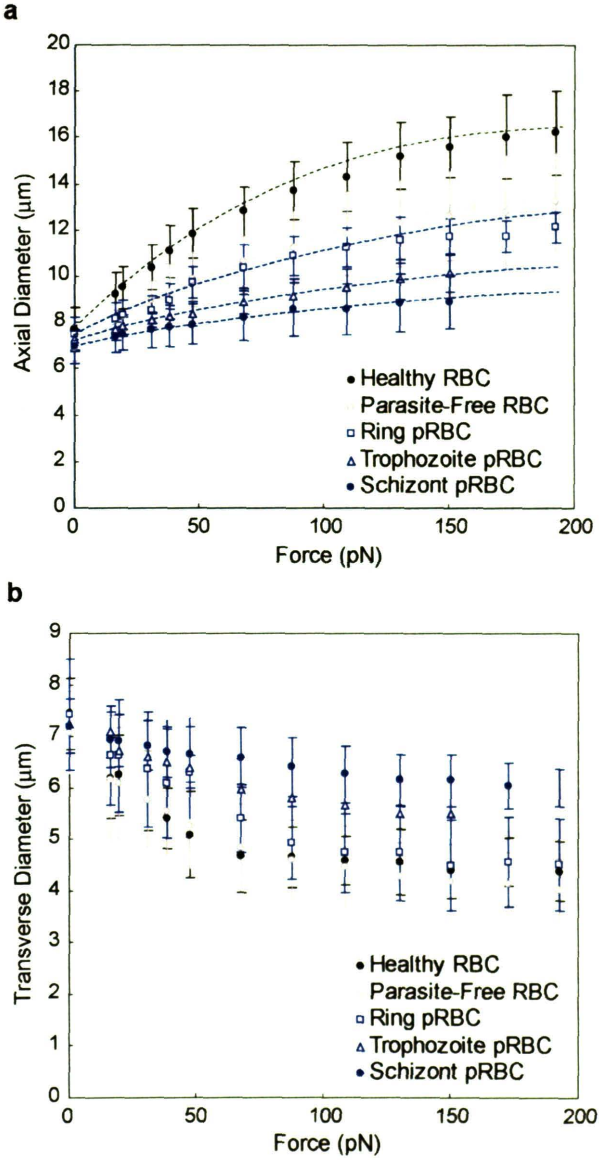

Figure 5-2: Force–displacement data from optical tweezers tests on RBCs and pRBCs at each intra-erythrocytic parasite developmental stage. The (**a**) axial diameter increase and (**b**) transverse diameter decrease is measured from uniaxial tension tests of single RBCs or pRBCs. Data points are averages from repeat experiments for each test condition: healthy RBCs (7 samples), parasite–free RBCs (8), ring stage pRBCs (5), trophozoite stage pRBCs (5) and schizont stage pRBCs (23). The scatter bars represent the range of force–displacement responses measured for each condition. Progressive loss of deformability is captured by the changes in force–displacement response with intra–erythrocytic parasite maturation from ring stage to trophozoite stage to schizont stage. The dotted lines denote predicted variations of the axial diameter as a function of applied uniaxial force, based on three–dimensional finite element simulations described in Section 3.3. The RBC and pRBC membrane shear modulus values are extracted from the simulations that predict the experimentally measured force–displacement data for each test condition. This figure is adapted from Suresh *et al.* [6]

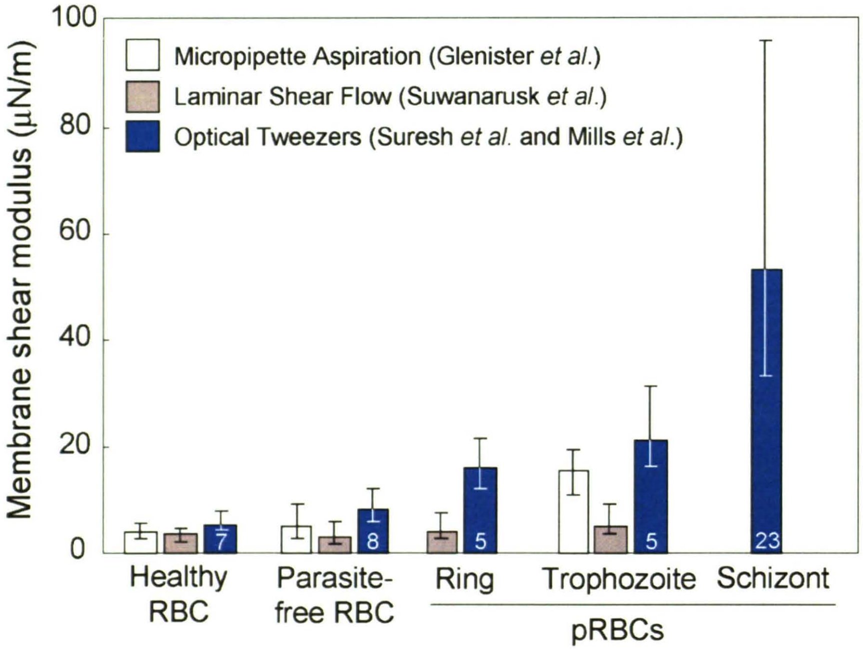

Figure 5-3: Measured RBC and pRBC membrane shear modulus values extracted from the force–displacement data presented in Figure 5-2 is compared to previous estimates by micropipette aspiration [7] and laminar shear flow [8] methods. (Shear modulus values plotted are based on analysis assuming that the membrane maintains constant volume, not the classical assumption of constant membrane area, as described in Section 3.3.) Bars represent average measurement and scatter bars indicate the range of measurements for a given condition. The average values of membrane shear modulus determined by optical tweezers uniaxial tension tests (black bars) are 5.3 μN/m (for healthy RBCs), 8 μN/m (parasite-free RBCs), 16 μN/m (ring stage pRBCs), 21 μN/m (trophozoite stage pRBCs) and 53 μN/m (schizont stage pRBCs). Optical tweezers, used in the present study, is the only technique able to measure schizont stage pRBC deformability. The numbers on each bar indicate the number of samples tested for the given condition. This figure is adapted from Suresh *et al.* [6] and Mills *et al.* [9].

imental techniques involving micropipette aspiration [7] and laminar shear flow [8] for *P. falciparum* pRBCs. Key observations made from the information shown in Figure 5-3 for *P. falciparum* pRBCs are provided below:

- The optical tweezers method is capable of providing the elastic deformation characteristics of the RBCs schizont stage infection, which prior methods [7, 8, 39, 40] based on micropipette aspiration and laminar shear flow could not capture because of enhanced pRBC rigidity and novel pRBC adhesion properties.
- Estimates extracted from the present optical tweezers experiments point to substantially (by up to three to four times) greater stiffening of *P. falciparum* pRBCs than previously anticipated [7]. The elastic shear modulus values for ring stage pRBCs, trophozoite stage pRBCs and schizont stage pRBCs are 16, 21 and 53 μN/m, respectively.
- The shear modulus of schizont stage pRBCs is up to an order of magnitude higher than that of healthy RBCs (median healthy RBC shear modulus is 5.3 μN/m (see Fig. 5-3); $p = 0.00011$[3]). Schizont stage pRBCs also undergoes a shape change to a sphere compared to the biconcave (discocyte) shape of a healthy RBC[4]. The spherical shape is also less conducive to severe deformation at large strains because of its weakened deformability due to lower surface to volume ratio and because its membrane does not fold as in the case of the discocyte shaped cell [4, 25].

When the applied force imposed on an RBC or pRBC is released, the cell fully relaxes to its original shape. From video images of such relaxation, the characteristic time of relaxation can be estimated. Optical tweezers studies of healthy RBCs [4, 25] measure the characteristic relaxation time to be 0.19 ± 0.06 s; corresponding literature value estimated from micropipette experiments is $0.10 - 0.30$ s [26]. No significant differences in the viscoelastic response, over and above the experimental scatter, could be identified for the

---

[3] The statistical significance between different test conditions was assessed by p–value statistics based on Mann-Whitney U tests. The compared measure between test conditions was the percent elongation in the axial direction at 108 pN of force. Comparing healthy RBCs and schizont stage pRBCs, the small p–value ($0.00011 < 0.05$) indicates a statistically significant difference between medians in the data sets. No comparison between medians of data sets were made when p–values were greater than 0.05

[4] The sphere shape of schizont stage pRBCs is taken into account in the FEM analysis.

ring and trophozoite pRBCs. The small deformations applied to schizont stage pRBCs did not allow accurate measurement of the characteristic relaxation time. It is noted that the original geometry of schizont stage pRBCs is recovered within a fraction of a second.

There is evidence indicating that exo-antigens released from mature parasites in pRBCs could increase the stiffness of parasite–free RBCs [39, 61]. Consistent with this expectation, our experiments show that the average stiffness of parasite–free RBCs is 8 μN/m compared to the value of 5.3 μN/m for healthy RBCs (see Fig. 5-3).

Structure-property-biology connections for *P. falciparum* parasitized RBCs

The significant increase in membrane shear modulus of RBCs due to *P. falciparum* parasitization (Fig. 5-3) can arise partly from the mere presence of a parasite inside a pRBC which can undergo nuclear division in the late schizont stage to produce as many as 20 merozoites. The continual structural changes occurring during the asexual blood stage of the parasite are also accompanied by changes to the cell membrane and cytoskeleton [2, 17]. The study of hereditary haemolytic anaemia has long provided insights into the organization of sub-membranous cytoskeletal proteins and their molecular architecture [2, 7], from which three broad inferences can be extracted:

- protein-protein and protein–lipid interactions greatly influence the correct assembly of the membrane cytoskeleton
- the cortical skeleton mostly determines the discocytic shape of the RBC and its deformability, and
- changes to the cytoskeletal chemistry and architecture can produce significant alterations to the RBC shape, elastic properties and rheological response.

In normal RBCs, membrane mechanical properties are mostly governed by the sub-membrane protein architecture whose principal components comprise alpha- and beta-spectrin, actin, proteins 4.1 and 4.2, adducin, dematin, protein 3 and its partner ankyrin. Attachments between the membrane and cytoskeleton are facilitated by chemical interactions involving ankyrin and the RBC anion transporter as well as protein 4.1 and glycophorin A [2, 7, 17]. Alterations to this delicate molecular architecture due to abnormalities that mediate cross-linking of cytoskeletal proteins can result in severe mechanical property changes to the the RBC membrane. When a *P. falciparum* parasite matures inside a pRBC, several parasite proteins are introduced into the RBC membrane and cytoskeleton, altering its mechanical response and adhesive properties. Among these proteins, *P. falciparum* ring-infected erythrocyte surface antigen (RESA), knob-associated histidine-rich protein (KAHRP) and *P. falciparum* erythrocyte membrane protein 3 (PfEMP3) are exported to the pRBC membrane by the parasite. Genetic methods to knock out *KAHRP* and *PfEMP3* with transgenic parasite clones have provided means for systematically characterizing the individual contributions of specific proteins to the increase in modulus of pRBCs. Figure 5-4 shows measurements of membrane shear modulus by micropipette aspiration for healthy RBC, parasite–free RBC, wild–type knobby clone (3D7) pRBC, knobby clone *PfEMP3* knock out (*EMP3*–KO) pRBC and knobless *KAHRP* knock out (*K*–KO) pRBC, obtained by Glenister *et al.* [7]. It is inferred from these results that KAHRP and PfEMP3 each contribute about 50% and 15%, respectively, to the overall increase in membrane shear modulus of pRBCs.

The pronounced increase in rigidity of *P. falciparum* pRBCs has important consequences for biological functions. RBCs coated with an antibody or having impaired deformability due to membrane proteins or intracellular particulates can be removed by the spleen. *P. falciparum* pRBCs begin to adhere to vascular endothelium after the ring stage (about 24 h after RBC invasion), thereby avoiding removal by spleen [62, 63]. Thus, how *P. falciparum* matures inside a pRBC leads to severe malaria could be in part linked to changes in pRBC mechanical properties, in addition to other pathogenic components such as uncontrolled systemic inflammatory process. To illustrate this connection, the effects on pRBC deformability caused by *P. falciparum* are contrasted with those of *P. vivax.* Although these two species of *Plasmodium* are equally prevalent in Southeast Asia, the former is responsible for essentially all malaria–related mortality whereas the latter is relatively benign. Experiments [8] based on a laminar shear flow method reveal deformability of *P. vivax* pRBCs is greater than that of healthy RBCs (with pRBC membrane shear modulus at the amoeboid stage decreasing by 50% from that of healthy RBCs), in contrast to the opposite behavior exhibited by *P. falciparum* pRBCs. Furthermore, the surface area of *P. vivax* pRBCs at a mature stage is twice that of a healthy RBC. These results suggest the

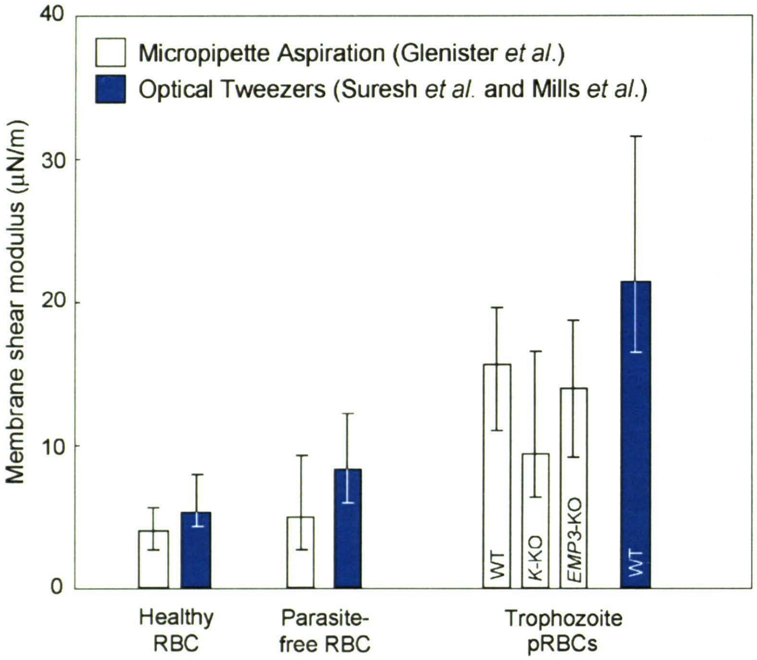

Figure 5-4: Results from the work of Glenister *et al.* [7] (white bars) showing the effect of mature stage exported proteins EMP3 and KAHRP on pRBC deformability at mature stages based on *EMP3* and *KAHRP* knock out parasites derived from knobby 3D7 *P. falciparum*. For comparison, experimental results on 3D7 from the present study (Fig. 5-3) are also provided (black bars).

possibility that increasing deformability and surface area protects *P. vivax* pRBCs (*P. vivax* targets young RBCs, reticulocytes, for invasion) by allowing circulation unhindered through the intercellular gaps in the sinusoids of the spleen, thereby avoiding splenic entrapment and removal.

5.3 Summary

By employing optical tweezers tests, the first continuous and direct force–displacement curves for pRBCs as a function of the intra–erythrocytic developmental parasite stage are presented. A gradual stiffening of the RBC membrane occurs as the parasite develops from the ring to the trophozoite to the schizont stage. For the case *P. falciparum* pRBCs, up to a 10-fold increase in membrane shear modulus is shown for the advanced stages of intra–erythrocytic development compared to healthy RBCs. *P. falciparum* pRBCs, which are significantly stiffened during intra–erythrocytic parasite development, sequester in the microvasculature and contribute to compromised blood flow to tissues. The stiffening of pRBCs is ascribed to specific proteins transported from the parasite surface to the cell membrane [38].

Chapter 6

Effect of Plasmodial RESA Protein on *P. falciparum* Parasitized Red Blood Cell Deformability

6.1 Introduction

During intra–erythrocytic development, *P. falciparum* exports proteins that interact with the host cell plasma membrane and sub–plasma membrane–associated spectrin network. Parasite exported proteins modify mechanical properties of parasitized RBCs (pRBCs), resulting in altered cell circulation. In this chapter, optical tweezers (described in Section 3.2.2) were used to investigate the effect of Pf155/Ring–infected Erythrocyte Surface Antigen (RESA), a parasite protein transported to the host spectrin network, on deformability of ring stage pRBCs. Using a set of parental, gene disrupted and revertant isogenic clones, it was found that RESA plays a major role in reducing deformability of pRBCs at the ring stage of intra–erythrocytic parasite development, but not at more advanced stage. It is also shown that the effect of RESA on deformability is more pronounced at febrile temperature, which ring stage pRBCs can be exposed to during a malaria attack, than at normal body temperature.

Following *P. falciparum* merozoite invasion of a RBC, the parasite differentiates and multiplies for 48 h, leading to rupture of the pRBCs and release of new merozoites in the blood circulation. Throughout this 48 h period, several parasite proteins are introduced into the RBC plasma membrane and sub-membranous protein skeleton, thereby modifying a range of structural and functional properties of the pRBCs [6, 17, 39, 40]. The best documented changes occur as *P. falciparum* matures to the trophozoite (24 – 36 h) and schizont (36 – 48 h) stages. During these stages pRBCs display decreased membrane deformability [6, 7, 9, 39, 40, 56], become spherical and develop cytoadherence properties responsible for parasite sequestration in the post–capillary venules of different organs [2, 62]. In contrast, during early parasite development, ring stage (0 – 24 h post–invasion) pRBCs preserve their biconcave shape, can circulate in peripheral blood [64] and thus are exposed to the spleen red pulp. Ring stage pRBCs may pass through this spleen compartment, be expelled from circulation, or return to the circulation once the parasite has been removed [65]. Although the relative importance of these different processes and their underlying mechanisms are not fully understood, it is likely that membrane stiffening of ring stage pRBCs [9] plays a crucial role in determining pRBCs spleen processing.

Introduction of parasite components within the pRBC membrane and cortical cytoskeleton begins soon after RBC invasion, as demonstrated for the well–characterized parasite protein Pf155/RESA [66]. This protein is discharged by the invading merozoite and exported to the pRBC membrane where, once phosphorylated, it interacts with the spectrin network [61]. Because spectrin plays a critical role in the ability of RBCs to deform [67, 68], it has been proposed that RESA could play an important role in the modulation of mechanical properties of ring stage pRBCs [17, 56]. A connection between RESA and altered pRBC mechanical properties was demonstrated in a previous study on pRBC membrane stability. *resa1*–KO pRBCs obtained by gene disruption were prone to heat–induced vesiculation when exposed at 50°C, whereas *resa1*+ pRBCs were not [69]. This observation confirmed previous conjectures about the stabilization effect of RESA on the RBC sub–membranous cytoskeleton against heat–induced structural changes [70]. However, analysis of RBC membrane deformability using a micropipette approach was not able to resolve any significant modification of membrane mechanical properties due to RESA[69].

Recently, optical tweezers have been used to characterize changes in the mechanical

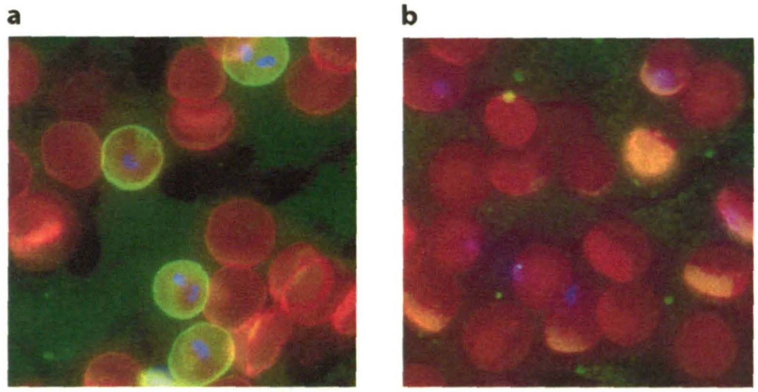

Figure 6-1: Immunofluorescence images of *P. falciparum* pRBCs: Band 3 labeled in red; parasite labeled in purple; RESA labeled in green. (**a**) Wild type pRBCs at the ring stage show RESA present at the RBC membrane. (**b**) *resa1*-KO pRBCs obtained by gene disruption did not express any detectable RESA protein.

properties of *P. falciparum* pRBCs [6, 9]. Here this methodology is used to readdress the question of the role of RESA on RBC deformability. To ascertain the role of RESA, a set of three isogenic cloned parasite lines were constructed: a *resa1* wild type, a *resa1*-KO targeted gene disruptant clone and the *resa1+* revertant of this clone. Immunofluorescence imaging confirms that RESA associates with the RBC membrane for the wild type case and is absent for the *resa1*-KO targeted gene disruptant clone (Fig. 6-1). Tests were conducted at room temperature to comply with standard deformability assays, as well as at 37°C and 41°C to investigate possible effects on deformability resulting from febrile temperature to which ring-stage pRBCs are exposed during a malaria attack. The results presented in this Chapter are also reported in a submitted manuscript [10].

6.2 Results and Discussion

Effect of RESA protein on ring stage pRBC deformability

Measurement of modulus values for pRBCs were performed on late ring stage pRBCs (14 – 20 h post invasion) harboring wild type *resa1+*, *resa1*-KO and *resa1*-rev parasites[1].

---

[1] **Plasmid constructs and gene disruption:** PCR amplified full length *P. falciparum* resa1 gene

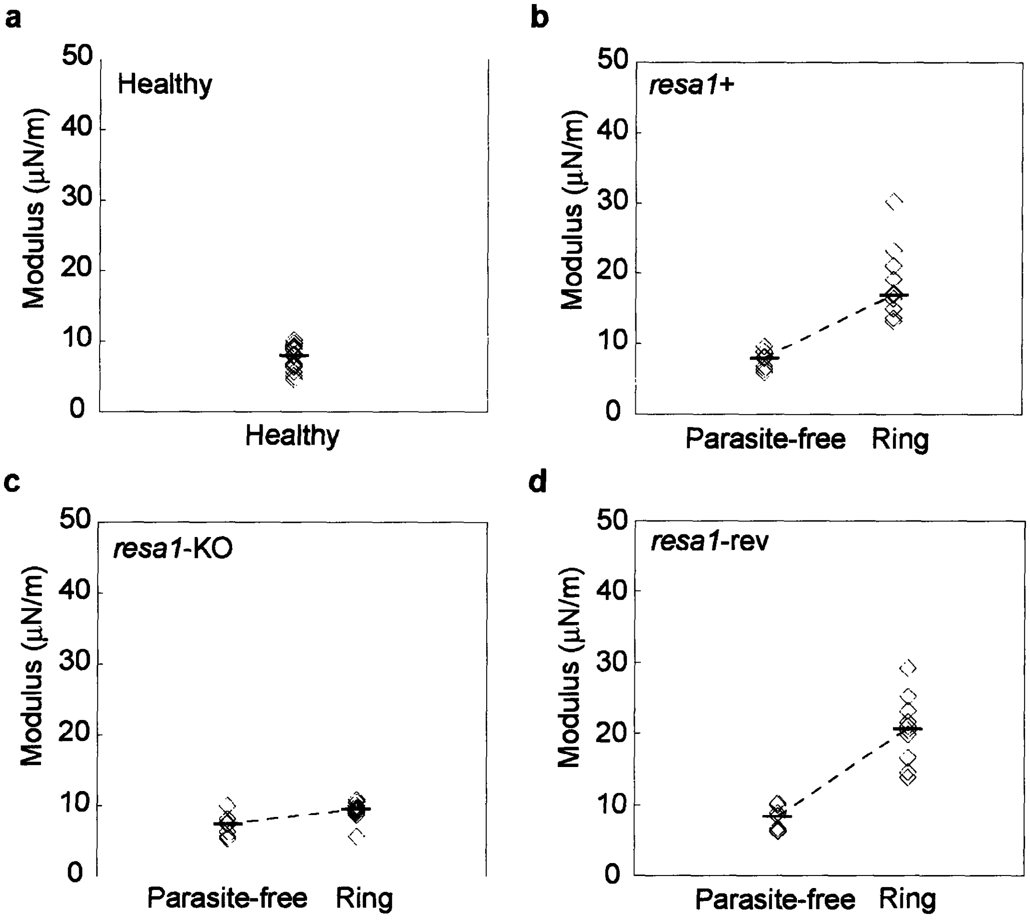

Figure 6-2: Deformability of control, parasite-free and late ring stage (14 – 20 h post invasion) pRBCs at room temperature (25°C). Tests were performed on cultures of (**a**) control RBCs, (**b**) wild-type *resa1+* pRBCs, (**c**) *resa1*-KO pRBCs and (**d**) *resa1*-rev pRBCs. This figure was adapted from a submitted manuscript [10]

Control tests were performed on healthy RBCs maintained under standard pRBC culture conditions and parasite–free RBCs that were present in pRBC cultures but did not harbor any parasites. Deformability tests were first performed at room temperature (25°C) (Fig. 6-2). Consistent with earlier work based on micropipette aspiration [5] and optical tweezers [4], the measured modulus of healthy RBCs was $5 - 10$ μN/m ($\mu = 6.8$ μN/m)[2] (Fig 6-2a). The deformability of late ring stage *resa1+* pRBCs ($\mu = 17.7$ μN/m) (Fig. 6-2b) decreased significantly compared to healthy RBCs ($p < 0.0001$)[3]. The two–fold increase in membrane modulus for *resa1+* pRBCs is consistent with previous work using 3D7, a *resa1+ P. falciparum* clone [6, 9]. In contrast, late ring stage *resa1*–KO pRBCs ($\mu = 9.4$ μN/m) (Fig. 6-2c) did not display decreased deformability compared to healthy RBCs. The observed deformability of *resa1*–KO pRBCs was significantly different compared to wild type *resa1+* pRBCs ($p < 0.0001$).

In order to ensure that targeted gene disruption of *resa1* (and hence the absence of RESA) and not another effect was responsible for the deformability observed in *resa1*–KO pRBCs, *resa1*–rev pRBCs were tested (Fig. 6-2d). The measured deformability of *resa1*–rev pRBCs ($\mu = 20.8$ μ N/m) was similar to that of the *resa1+* pRBC and showed a significantly higher modulus compared to healthy RBCs ($p < 0.0001$) or *resa1*–KO pRBCs ($p < 0.001$). Parasite-free RBCs from wild type *resa1+*, *resa1*–KO and *resa1*–rev parasite

---

was cloned in between SacII/XbaI sites of a modified pdTg23 vector [71] carrying the Toxoplasma gondii dihydrofolate reductase/thymidine synthase gene dhfr/ts (conferring resistance to pyrimethamine) fused in frame with the herpes virus thymidine kinase 1 [72, 73]. Ring stage FUP/CB (resa1+) clone parasites (FCR3-resa1+ like genotype) were transfected with 100 g of QIAGEN-purified targeting plasmid using the electroporation conditions described in [74]. Homologous recombination in the endogenous resa1 gene was obtained following a 2 step pyrimethamine pressure selection [71]. Pyrimethamine-resistant parasites were cloned by limiting dilution. 10 M ganciclovir drug pressure was applied on genetically confirmed resa1–KO parasites in absence of pyrimethamine to induce the resa1 gene reversion (resa1–rev parasites) [73]. The development of gene disrupted parasites used for results in this chapter are described in Diez Silva *et al.* [69] and the Ph.D. thesis of Diez Silva [75].

Parasite culture: A clone derived from *P. falciparum* (FUP/CB) parasites, named here wild type resa1+ *P. falciparum* was maintained in leukocyte-free human O+ erythrocytes (Research Blood Components, USA), stored at 4°C for no longer than two weeks, under an atmosphere of 3% 0_2, 5% CO_2 and 92% N_2 in RPMI 1640 medium (Gibco Life Technologies) supplemented with 25 mM HEPES (Sigma), 200mM hypoxanthine (Sigma), 0.209% $NaHC0_3$ (Sigma) and 0.25% albumax I (Gibco Life Technologies). Cultures were synchronized successively by concentration of mature schizonts using plasmagel flotation [76] and sorbitol lysis two hours after the merozoite invasion to remove residual schizonts [77]. For wild type resa1+, resa1–KO and resa1–rev Pf-RBCs tests, optical tweezers deformability tests were performed within and $14 - 20$ h (ring stage) or $24 - 36$ h (trophozoite stage) after merozoite invasion. Parasite culture was performed by M. Diez Silva.

[2] The RBC or pRBC membrane shear modulus, μ, reported in this chapter corresponds to the median value based on multiple samples.

[3] p–values are calculated by two–tailed Mann-Whitney rank sum tests comparing modulus values between indicated test conditions.

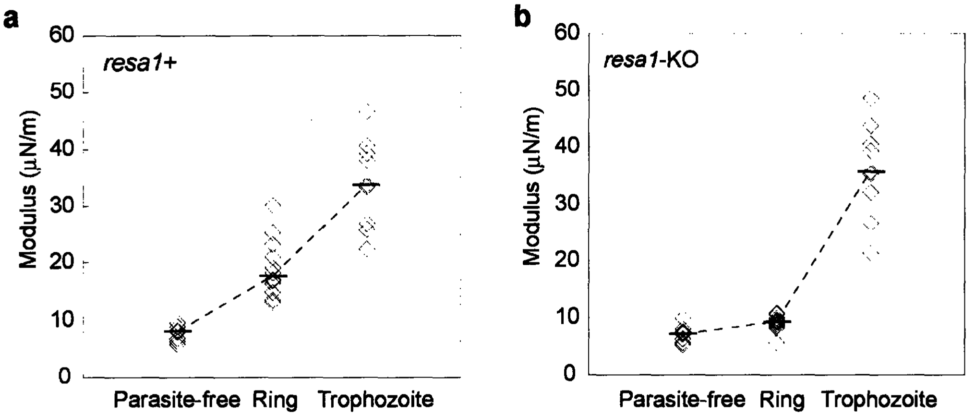

Figure 6-3: Deformability over progressive parasite maturation from ring (12 – 24 h post-invasion) to the trophozoite stage (24 – 36 h post-invasion) at room temperature (25°C). Tests were performed on cultures of (a) wild-type *resa1+* pRBCs and (b) *resa1*-KO pRBCs.

cultures (Fig. 6-2b–d, respectively) displayed similar levels of deformability compared to healthy RBCs (Fig. 6-2a).

Effect of RESA protein on trophozoite stage pRBC deformability

To determine whether the presence of RESA protein at the ring stage is needed for implementing the changes of the mechanical properties displayed by subsequent mature stages of pRBCs, the deformability of *resa1+* and *resa1*-KO trophozoite stage pRBCs (24 – 36 h post invasion) was measured. The deformability of trophozoite stage *resa1+* (μ = 35.9 μN/m) and *resa1*-KO (μ = 35.7 μN/m) pRBCs (Fig. 6-3) were significantly lower than ring stage *resa1+* pRBCs ($p < 0.001$) and *resa1*-KO ($p < 0.001$), respectively. The four–fold increase in modulus measured for both *resa1+* and *resa1*-KO trophozoite stage pRBCs is consistent with previous studies [6, 9]. No difference in deformability between *resa1+* and *resa1*-KO pRBCs was observed at the trophozoite stage.

Impact of physiological temperatures on ring stage pRBC deformability

To study pRBC deformation at physiological temperature and the consequences of elevated body temperature during febrile malaria episodes, deformability tests on *resa1+* and *resa1*-KO ring stage pRBCs were carried out at normal body temperature (37°C) and

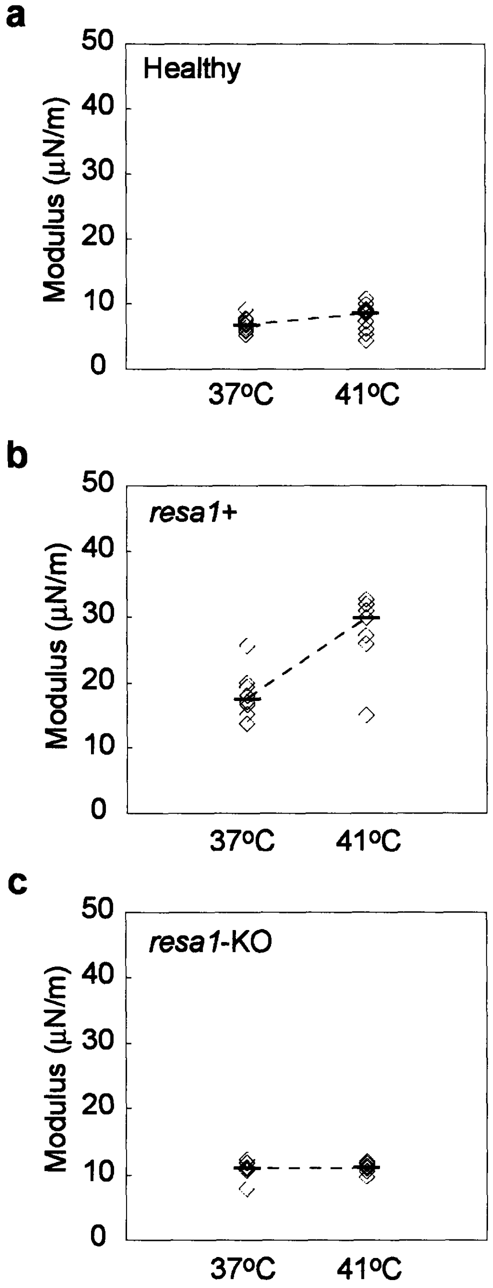

Figure 6-4: Deformability of RBCs and pRBCs at normal body (37°C) and febrile (41°C) temperatures. Tests were performed on cultures of (a) healthy RBCs, (b) wild-type *resa1*+ pRBCs and (c) *resa1*–KO pRBCs.

febrile temperature (41°C) (Fig. 6-4a). The modulus of healthy RBCs at 37°C (μ = 6.6 μN/m) and 41°C (μ = 8.6 μN/m) was similar to deformability of healthy RBCs at room temperature ($\mu = 5 - 10$ μN/m) (Fig. 6-2a). The observation that deformability of healthy RBCs remains approximately constant over this temperature range is consistent with similar measurements using micropipette aspiration [5] and results presented in Chapter 4 by optical tweezers.

Ring stage *resa1+* pRBCs displayed a marked decrease in deformability both at 37°C (μ = 17.6 μN/m) and 41°C (μ = 29.9 μN/m) (Fig. 6-4b) compared to healthy RBCs. The deformability decrease for *resa1+* pRBCs was significantly greater at 41°C than at 37°C ($p < 0.05$). In contrast, the deformability of *resa1*–KO pRBCs (Fig. 3c) at 37°C ($\mu = 11$ μN/m) and 41°C (μ = 11.2 μN/m) remained similar to measurements at room temperature (μ = 9.4 μN/m) (Fig. 6-2c).

During intra–erythrocytic development of *P. falciparum*, parasite exported proteins contribute to modifications of the deformability of pRBCs. The contribution of specific parasite exported proteins to decreased deformability has been demonstrated for KAHRP and PfEMP3 [7], which are present in the erythrocyte membrane in the trophozoite and schizont stages when pRBCs are sequestered. The present study explores the effect of RESA, a ring stage parasite exported protein, on altered deformability of pRBCs that are not sequestered and, therefore, must navigate the circulation. We document here a significantly reduced deformability of ring stage pRBCs and show that RESA is largely responsible for this mechanical property change. While measured deformability of healthy RBCs remained constant over all test temperatures, decreased deformability of ring stage pRBCs was greater at febrile temperature than normal body temperature. Since *resa1*–KO pRBCs exhibited deformability similar to healthy RBCs at all temperatures, we conclude that the temperature–related change in membrane deformability is attributable, at least in part, to the presence of RESA in the ring stage pRBC membrane. At the more advanced trophozoite stage, decreased deformability of pRBCs was independent of a parasite's ability to express RESA. It has been shown that RESA can no longer be detected at the trophozoite stage [78], where parasite proteins other than RESA play a predominant role in decreased deformability. Furthermore, the present results indicate that absence of RESA in ring stage does not impair subsequent remodeling in the late parasite stages. Altered deformability during the ring stage is most probably a consequence of the attachment of RESA to spectrin [79]. Binding of RESA to R16 spectrin structural repeat close to the interaction region between $\alpha 1$ and $\beta 1$ spectrins significantly increases the stability of spectrin tetramers [80]. In healthy RBCs, the spectrin network exists in a dynamic state of spectrin tetramers dissociating transiently into dimers and shear deformation shifts the equilibrium of tetramer formation toward the dissociated dimer state [81]. Thus, RESA stabilization of tetramers could modify spectrin network dynamic properties thereby impairing on membrane deformability. This model is consistent with a proposed role for RESA on temperature–dependant membrane stability. Increased membrane resistance to thermal shift–induced structural change has been related to the stabilization of spectrin tetramers induced by RESA binding [80]. Although the effect of temperature on the interaction between RESA and spectrin is unknown, we speculate that this specific binding alters temperature–dependent stabilization of spectrin tetramers and, as a consequence, contributes to the observed changes in ring stage pRBCs deformability at febrile temperatures.

Deformability is critical for *in vivo* parasite survival during the ring stage when pRBCs have not yet cytoadhered/sequestered and circulate in post–capillary microvessels and through the spleen. It is shown that ring stage pRBC decreased deformability is mediated/modulated by RESA, which binds to the RBC cytoskeleton. Moreover, the effect of RESA on deformability is greater at febrile temperature. It has been shown previously that exposure of ring stage pRBCs to febrile temperature negatively impacts parasite growth in the absence of RESA [69]. RESA may thus play a role in the delicate balance between parasite and its host during the ring stage, possibly through contributing to parasite resistance to febrile temperatures and through membrane deformability changes that may affect spleen–processing of the pRBC.

6.3 Summary

To characterize the role of RESA on deformability of ring and trophozoite stage pRBCs, the single-cell force–displacement response of healthy RBCs, wild-type *P. falciparum* pRBCs and gene disrupted *P. falciparum* pRBCs were evaluated by the trap stiffness optical tweezers method. The combination of gene disruption techniques and optical tweezers experiments enables the study of protein-level contributions to membrane deformability changes induced by *P. falciparum.* Ring stage pRBC decreased deformability was found to be significantly mediated/modulated by RESA. pRBCs parasitized by *resa1*-KO parasites had deformability similar to healthy RBCs, unlike wild-type *P. falciparum* pRBCs which stiffened two-fold compared to healthy RBCs. By testing trophozoite stage pRBCs, RESA was found to not play an accessory role in further loss of deformability associated with the mature parasite stages. The effect of RESA was found to be greater at febrile temperature, which ring stage pRBCs can be exposed to during a malaria attack, than at normal body temperature.

Chapter 7

Conclusions

The deformability of healthy and pathologic RBCs was investigated by measuring single–cell RBC mechanical properties. Two optical tweezers instruments were developed to conduct RBC deformability tests along with assays of specific molecular contributions that involved gene disruption of parasite proteins exported to the RBC membrane. Key conclusions of this thesis are presented in this chapter.

To experimentally determine the force–displacement response of single RBCs in uniaxial tension, two optical tweezers instruments were developed. Contributions of this work include:

- Through new escape force optical tweezers experimental data, calibration methods and three-dimensional computational modeling, it is shown that direct *in vitro* force–displacement relationships to large strains for human RBCs can be obtained reproducibly. The RBC membrane shear modulus values obtained by this optical tweezers method are consistent with accepted values based on a standard micropipette aspiration technique.

- A trap stiffness method optical tweezers instrument was developed. The force–displacement results from this technique were found to be equivalent to those obtained by the escape force method optical tweezers instrument. The trap stiffness method has advantages over the escape force method of being able to generate force–displacement curves from a single stretch in real-time with improved accuracy. In addition, the trap stiffness method opens up opportunities to interrogate time-dependent mechanical properties of single RBCs (e.g. stress relaxation, cyclic loading, strain rate tests). These capabilities of the new experimental tools developed in this work have been demonstrated through preliminary tests.

- Combining optical tweezers experiments with genetic disruption techniques allows investigation of single-protein level contributions to mechanical properties. These experiments provide fundamental understanding of causative factors that influence membrane deformability under pathologic conditions.

The mechanical properties of healthy RBCs were studied by escape force method optical tweezers experiments. Contributions of this work include:

- The shear modulus of healthy RBCs from three separate sets of experiments measured nominal shear modulus values of 7.3, 8.5, 5.3 μN/m. These results are consistent with the range of accepted shear modulus values based on micropipette aspiration experiments.
- Increasing the test temperature to physiological temperatures found no effect of temperature on RBC membrane shear modulus values, which was consistent with micropipette aspiration results over the same temperature range. However, temperature was found to play a significant role in how specific proteins influence RBC deformability upon parasite invasion.

An escape force optical tweezers method was used to measure the altered deformability of *P. falciparum* parasitized RBCs. This work presents the first continuous and direct force–displacement curves for the *P. falciparum* parasitized RBCs as a function of parasite developmental stage. Contributions of this work include:

- The increase in shear modulus over all intra–erythrocytic parasite developmental stages was characterized. Parasitized RBC membrane shear modulus values were found to increase from 16 μN/m (ring stage) to 21 μN/m (trophozoite stage) to 53 μN/m (schizont stage).

- A 10-fold increase in in-plane shear modulus in the advanced stages of intracellular parasite development compared to the healthy RBCs is shown. This value extracted from the present optical tweezers experiments point to substantially (by up to three to four times) greater stiffening of the RBCs from *P. falciparum* parasitization than previously anticipated. The large membrane stiffening coupled with a geometrical shape change to a sphere results in dramatically reduced deformability properties of schizont stage *P. falciparum* parasitized RBCs.

The effect of parasite exported protein RESA on deformability changes observed in *P. falciparum* parasitized RBCs was investigated by a trap stiffness method optical tweezers instrument. Contributions of this work include:

- It is shown that decreased deformability of ring stage *P. falciparum* parasitized RBCs is mediated/modulated by RESA, which binds to the RBC spectrin network. Deformability is critical for *in vivo* parasite survival during the ring stage when parasitized RBCs have not yet cytoadhered/sequestered and circulate in post-capillary microvessels and through the spleen.
- It is found that the effect of RESA on deformability is greater at febrile temperature. It has been shown previously that exposure of ring stage *P. falciparum* parasitized RBCs to febrile temperature negatively impacts parasite growth in the absence of RESA. RESA may thus play a role in the delicate balance between parasite and its host during the ring stage, on the one hand through contributing to parasite resistance to febrile temperatures and on the other hand through membrane deformability changes that may affect spleen-processing of the parasitized RBC.

Bibliography

[1] B. Alberts, A. Johnson, J. Lewis, M. Raff, K. Roberts, and P. Walter. *Molecular Biology of the Cell.* Taylor & Francis Group, Ltd., Oxford, UK, 2002.

[2] L. H. Miller, D. I. Baruch, L. Marsh, and O. K. Doumbo. *Nature*, 415:673, 2002.

[3] K. Svoboda and S. M. Block. *Ann. Rev. of Biophys. and Biomol. Str.*, 23:247, 1994.

[4] J. P. Mills, L. Qie, M. Dao, C. T. Lim, and S. Suresh. *Mol. and Cell. Biomech.*, 1(3):169, 2004.

[5] R. Waugh. PhD thesis, Duke University, Durham, 1977.

[6] S. Suresh, J. Spatz, J. P. Mills, A. Micoulet, M. Dao, C. T. Lim, M. Beil, and T. Sefferlein. *Acta. Bio.*, 1:16, 2005.

[7] F. K. Glenister, R. L. Coppel, A. F. Cowman, N. Mohandas, and B. M. Cooke. *Blood*, 99:1060, 2002.

[8] R. Suwanarusk, B. M. Cooke, A. M. Dondorp, K. Silamut, J. Sattabongkot, N. J. White, and R. Udomsangpetch. *Infect. Diseases*, 189:190, 2004.

[9] J. P. Mills, L. Qie, M. Dao, K. S. W. Tan, C. T. Lim, and S. Suresh. *Mater. Res. Soc. Symp. Proc.*, 844, 2005.

[10] J. P. Mills, M. Diez Silva, D. J. Quinn, M. Dao, K. S. W. Tan, C. T. Lim, G. Milon, P. H. David, O. Mercereau-Puijalon, S. Bonnefoy, and S. Suresh. *Manuscript in Preparation*, 2006.

[11] S. Eber and S. E. Lux. *Seminars in Hematology*, 41:118, 2004.

[12] P. G. Gallagher. *Seminars in Hematology*, 41:142, 2004.

[13] J. Delaunay. *Seminars in Hematology*, 41:165, 2004.

[14] G. Brugnara. *J. of Pediatric Hematology Oncology*, 25:927, 2003.

[15] G. Bosman. *Cell. and Mol. Bio.*, 50:81, 2004.

[16] O. Galkin and P. G. Vekilov. *J. of Mol. Bio.*, 336:43, 2004.

[17] B. M. Cooke, N. Mohandas, and R. L. Coppell. *Adv. Parasitol.*, 50:1, 2001.

[18] Y. C. Fung. *Biomechanics: mechanical properties of living tissues.* Springer-Verlag, New York, USA, 1993.

[19] E. A. Evans. *Biophys. J.*, 1:27, 1983.

[20] E. A. Evans and R. Skalak. *Mechanics and Thermal Dynamics of Biomembranes.* CRC Press, Inc., Boca Raton, Florida, USA, 1980.

[21] E. A. Evans. *Biophys. J.*, 13:941, 1973.

[22] R. M. Hochmuth and R. E. Waugh. *Annu. Rev. Physiol.*, 49:209, 1987.

[23] H. Engelhardt and E. Sackmann. *Biophys. J.*, 54:495, 1988.

[24] J. C. Leliévre, C. Bucherer, S. Greiger, C. Lacombe, and V. Vereycken. *J. Phys. III France*, 5:1689, 1995.

[25] M. Dao, C. T. Lim, and S. Suresh. *J. Mech. Phys. Solids*, 51, 2003.

[26] D. Boal. *Mechanics of the Cell.* Cambridge University Press, Cambridge, U. K., 2002.

[27] E. Evans and R. M. Hochmuth. *Biophys. J.*, 16:1, 1976.

[28] S. Hénon, G. Lenormand, A. Richert, and F. Gallet. *Biophys. J.*, 76:1145, 1999.

[29] R. M. Simmons, J. T. Finer, S. Chu, and J. A. Spudich. *Biophys. J.*, 70:1813, 1996.

[30] R. M. Hochmuth. *Properties of Red Blood Cells. In Handbook of Bioengineering.* McGraw-Hill, Inc., New York, USA, 1987.

[31] D. E. Discher, D. H. Boal, and S. K. Boey. *Biophys. J.*, 75:1584, 1998.

[32] G. Lenormand, S. Hénon, A. Richert, J. Siméon, and F. Gallet. *Biophys. J.*, 81(1):43, 2001.

[33] J. Sleep, D. Wilson, R. Simmons, and W. Gratzer. *Biophys. J.*, 77:3085, 1999.

[34] K. H. Parker and C. P. Winlove. *Biophys. J.*, 77:3096, 1999.

[35] M. S. Z. Kelleymayer, S. B Smith, C. Bustamante, and H. L. Granzier. *J. of Str. Bio.*, 122:197, 1998.

[36] G. Bao and S. Suresh. *Nature Materials*, 2:715, 2003.

[37] K. J. Van Vliet, G. Bao, and S. Suresh. *Acta Mat.*, 51:5881, 2003.

[38] L. H. Bannister, J. M. Hopkins, R. E. Fowler, S. Krishna, and G. H. Mitchell. *Parasitol. Today*, 16:427, 2000.

[39] H. A. Cranston, C. W. Boylan, G. L. Carroll, S. P. Sutera, J. R Williamson, I. Y. Gluzman, and D. J. Krogstad. *Science*, 223:400, 1984.

[40] M. Paulitschke and G. B. Nash. *J. Lab. Clin. Med.*, 122:581, 1993.

[41] C. T. Lim, M. Dao, S. Suresh, C. H. Sow, and K. T. Chew. *Acta Mat.*, 52:4065, 2004.

[42] A. Ashkin, J. M. Dziedzic, and T. Yamane. *Nature*, 330:769, 1987.

[43] J. P. Mills *et al. Manuscript in Preparation*, 2007.

[44] M. J. Lang, P. M. Fordyce, A. M. Engh, K. C. Neumann, and S. M. Block. *Nature Methods*, 1(2):133, 2004.

[45] M. J. Lang, P. M. Fordyce, and S. M. Block. *J. of Bio.*, 2(1):6, 2003.

[46] J. C. Simo and K. S. Pister. *Comp. Methods in App. Mech. and Eng.*, 46:201, 1984.

[47] O. H. Yeoh. *Rubber Chem. Technol.*, 63:792, 1990.

[48] D. E. Discher, N. Mohandas, and E. A. Evans. *Science*, 266:1032, 1994.

[49] M. Dao, J. Li, and S. Suresh. *Mat. Sci. Eng. C*, C 26:1232, 2006.

[50] ABAQUS Inc. *ABAQUS Users Manual, Version 6.3.* ABAQUS, Inc., Pawtucket, R. I., USA, 2002.

[51] J. Li, M. Dao, C. T. Lim, and S. Suresh. *Biophys. J.*, 88:3707, 2005.

[52] R. Waugh and E. A. Evans. *Biophys. J.*, 26:115, 1979.

[53] R. M. Hochmuth, P. R. Worthy, and E. A. Evans. *Biophys. J.*, 26:101, 1979.

[54] C. Chien, K. L. P. Sung, R. Skalak, and S. Usami. *Biophys. J.*, 24:463, 1978.

[55] M. Puig de Morales-Marinkovic, K. T. Turner, J. P. Butler, J. J. Fredberg, and S. Suresh. *Submitted manuscript*, 2007.

[56] G. Nash, E. Obrien, E. Gordonsmith, and J. Dormandy. *Blood*, 74:855, 1989.

[57] D. Walliker, I. A. Quakyi, T. E. Wellems, T. F. McCutchan, A. Szarfman, W. T. London, L. M Corcoran, T. R. Burkot, and R. Carter. *Science*, 26:1661, 1987.

[58] H. H. Ang, C. K. Lam, and M. J. Wah. *Chemotherapy*, 42:318, 1996.

[59] W. Trager and J. B. Jensen. *Science*, 193:673, 1976.

[60] T. G. Smith, P. Lourenco, R. Carter, D. Walliker, and L. C. Ranford-Cartwright. *Parasitology*, 121:127, 2000.

[61] M. Foley, L. Tilley, W. H. Sawyer, and R. F. Anders. *Biochem. Parasitol.*, 46:137, 1991.

[62] A. M. Dondorp, P. A. Kager, J. Vreeken, and N. J. White. *Parasitol. Today*, 16:228, 2000.

[63] K. Chotivanich, R. Udomsangpetch, R. McGready, S. Proux, P. Newton, S. Pukrittayakamee, S. Looareesuwan, and N. J. White. *J. Infect. Diseases*, 185:1538, 2002.

[64] I. W. Sherman, S. Eda, and E. Winograd. *Microbes Infect.*, 5:897, 2003.

[65] B. J. Angus, K. Chotivanich, R. Udomsangpetch, and N. J. White. *Blood*, 90:2037, 1997.

[66] H. Perlmann, K. Berzins, M. Wahlgren, J. Carlsson, A. Bjorkman, M. E. Patarroyo, and P. Perlmann. *J. Exp. Med.*, 159:1686, 1984.

[67] V. Bennett and S. Lambert. *J. Clin. Invest.*, 87:1483, 1991.

[68] N. Mohandas and E. Evans. *Annu. Rev. Biophys. Biomol. Struct.*, 23:787, 1994.

[69] M. Diez Silva, B. M. Cooke, M. Guillotte, D. W. Buckingham, J. P. Sauzet, C. Le Scanf, H. Contamin, P. David, O. Mercereau-Puijalon, and S. Bonnefoy. *Mol. Microbiol.*, 56(4):990, 2005.

[70] E. Da Silva, M. Foley, A. R. Dluzewski, L. J. Murray, R. F. Anders, and L. Tilley. *Mol. Biochem. Parasitol.*, 66:59, 1994.

[71] Y. Wu, L. A. Kirkman, and T. E. Wellems. *Proc. Nat. Acad. Sci. USA*, 93:1130, 1996.

[72] A. C. Garapin, F. Colbere-Garapin, M. Cohen-Solal, F. Horodniceanu, and P. Kourilsky. *Proc. Nat. Acad. Sci. USA*, 78:815, 1981.

[73] S. Bonnefoy *et al. Manuscript in Preparation*, 2006.

[74] D. A. Fidock and T. E. Wellems. *Proc. Nat. Acad. Sci. USA*, 94:10931, 1997.

[75] M. Diez Silva. PhD thesis, Institut Pasteur, Paris, France, 2005.

[76] G. Pasvol, R. J. Wilson, M. E. Smalley, and J. Brown. *Ann. Trop. Med. Parasitol.*, 72:87, 1978.

[77] C. Lambros and J. P. Vanderberg. *J. Parasitol.*, 65:418, 1979.

[78] R. L. Coppel, S. Lustigman, L. Murray, and R. F. Anders. *Mol. Biochem. Parasitol.*, 31:223, 1988.

[79] M. Foley, L. Corcoran, L. Tilley, and R. Anders. *Exp. Parasitol.*, 79:340, 1994.

[80] X. Pei, X. Guo, R. Coppel, K. Haldar, W. Gratzer, N. Mohandas, and X. An. *Submitted*, 2006.

[81] X. An, M. C. Lecomte, J. A. Chasis, N. Mohandas, and W. Gratzer. *J. Biol. Chem.*, 277:31796, 2002.